Agricultural and Forest Meteorology 292–293 (2020) 108111

Contents lists available at ScienceDirect

Agricultural and Forest Meteorology

journal homepage: www.elsevier.com/locate/agrformet

Future greening of the Earth may not be as large as previously predicted

Qian Zhao[a], Zaichun Zhu[a,*], Hui Zeng[a,*], Weiqing Zhao[a], Ranga B. Myneni[b]

[a] School of Urban Planning and Design, Peking University Shenzhen Graduate School, Peking University, Shenzhen 518055, Guangdong, China
[b] Department of Earth and Environment, Boston University, Boston, MA 02215, USA

ARTICLE INFO

Keywords:
Vegetation greening
Leaf area index
Climate change
Reliability ensemble averaging
Earth system models
Shared socioeconomic pathways

ABSTRACT

Changes in global vegetation growth and its drivers during recent decades have been well studied with satellite data, ecosystem models and field experiments. However, a systematic understanding of how global vegetation will respond to projected changes in climate and atmospheric composition is still lacking. Here, we analyze changes in projected global leaf area index (LAI) from 16 Coupled Model Intercomparison Project phase 5 (CMIP5) and 17 phase 6 (CMIP6) Earth System Models (ESMs) during the 21st century under future scenarios RCP2.6, RCP4.5 and RCP8.5 and future scenarios SSP1–2.6, SSP2–4.5, SSP3–7.0 and SSP5–8.5, respectively. In addition to the widely-used multi-model ensemble mean (MME) method, we employed the Reliability Ensemble Averaging (REA) strategy to integrate the modeled results. The REA integration weights were determined by combining the performance of the ESMs in simulating present-day LAI changes, which was based on a comparison with three long-term remote sensing LAI data sets, with their convergence of future predictions. The results suggest that global LAI will increase under all seven future scenarios with both integration methods. The magnitude of LAI growth is expected to increase with the forcing levels of the scenarios. The ESMs integrated with the REA weights predicted significantly smaller magnitudes and lower uncertainties in global LAI growth by the end of the 21st century than those integrated with the MME method. Both REA and MME results suggest that the growth in atmospheric CO_2 concentration is the main positive driver of the projected increment of global LAI, which is partly offset by the negative effects of global warming. Our improved comprehensive prediction based on CMIP5 and CMIP6 ESMs using the REA integration strategy provides a more robust estimation of global vegetation change during the 21st century, and is expected to help better understand the state of the planet in the coming decades.

1. Introduction

Vegetation is a key component of the biosphere, not only providing food, fuel and fiber, but also mediating regional and global climate by absorbing carbon dioxide from the atmosphere, altering land surface roughness and changing the ratio of latent and sensible heat (Beer et al., 2010; Bonan, 2008; IPCC, 2013; Zeng et al., 2017). However, vegetation is sensitive to environmental conditions (Jung et al., 2017; Nemani et al., 2003), which have been changing remarkably since the industrial revolution (IPCC, 2013). For example, atmospheric CO_2 concentration and global temperature, the key environmental factors affecting vegetation growth, have increased by nearly 50% percent and nearly 1 °C since their preindustrial levels, respectively (IPCC, 2013). How vegetation responds to global environmental change has attracted lots of attention of the research community in recent years (Chen et al., 2019; Foley et al., 2005; Hovenden et al., 2019; Obermeier et al., 2017; Peñuelas et al., 2013; Zhu et al., 2017, 2016, 2018).

Remote sensing and ecosystem models are useful tools for investigating large-scale vegetation dynamics. Satellite records have consistently shown that global vegetation has been growing since the 1980s (Chen et al., 2019; Los, 2013; Myneni et al., 1997; Piao et al., 2006a; Zhou et al., 2003, 2001; Zhu et al., 2016). Current ecosystem models can, to some extent, reproduce the observed enhancements in vegetation growth. Combining remote sensing and ecosystem models provides an effective way to quantify the relative contribution of the environmental factors to the vegetation dynamics (Piao et al., 2006a; Zhu et al., 2017, 2016). Attribution of changes in vegetation growth using ecosystem models somewhat circumvent the "correlation does not

Abbreviations: (CMIP5), Coupled Model Intercomparison Project phase 5; (CMIP6), Coupled Model Intercomparison Project phase 6; (MME), Multi-model Ensemble Mean; (REA), Reliability Ensemble Averaging

* Corresponding authors.
E-mail addresses: zhaoqian7a@126.com (Q. Zhao), zhu.zaichun@pku.edu.cn (Z. Zhu), zengh@pkusz.edu.cn (H. Zeng), wqzhao@webmail.hzau.edu.cn (W. Zhao), ranga.myneni@gmail.com (R.B. Myneni).

https://doi.org/10.1016/j.agrformet.2020.108111
Received 14 April 2020; Received in revised form 17 July 2020; Accepted 20 July 2020

necessarily imply causation" and nonlinear problems that cannot be address by traditional statistical models (Lucht et al., 2002; Mao et al., 2013; Piao et al., 2006; Zhu et al., 2016). Ecosystem models have suggested that the greening of global vegetation has been mainly driven by increasing atmospheric CO_2 concentration, and that climate change and land use change are strong regional drivers of vegetation dynamics (Chen et al., 2019; Mao et al., 2016; Zhu et al., 2016).

Understanding how vegetation responds to past global environmental change is of great importance to help us better project the spatio-temporal change of global vegetation under future scenarios. Earth system models (ESMs) that are coupled with state-of-the-art ecosystem models provide a physically-based tool for projecting future terrestrial vegetation conditions under prescribed scenarios (Anav et al., 2013a, 2013b). The Climate Model Intercomparison Project phase 5 (CMIP5) coordinated dozens of ESMs that can simulate the pathways of global vegetation dynamics until the end of the 21st century under several prescribed Representative Concentration Pathways (RCPs) (Taylor et al., 2012). Recently, a portion of the Climate Model Intercomparison Project phase 6 (CMIP6) has been accomplished, providing an updated projection of future vegetation change (Eyring et al., 2016).

Current ESMs generally show large discrepancies in simulating global vegetation dynamics under future scenarios (Anav et al., 2013a, 2013b). The discrepancies between the ESMs originate from differences in their driving data, the model structure and the coupling strategy of the land, atmosphere and ocean modules (Anav et al., 2013a, 2013b). The multi-model ensemble mean (MME) approach is the most widely-used method for handling discrepancies among ESMs, helping to reduce the noises and highlight the signals from the ESMs outputs (IPCC, 2013; Zhu et al., 2016). The MME method treats all the individual ESM equally, i.e., all the models are integrated with the same weight regardless of their performance (Zhu et al., 2017). Several approaches have been proposed to overcome the problems that are introduced by the traditional "one vote per model" (Giorgi and Mearns, 2002b; Raftery et al., 2005; Vrugt et al., 2008; Zhu et al., 2017). These approaches consider the performance of each model and integrate their simulations in a more robust way. Specifically, the "Reliability Ensemble Averaging" (REA) method can improve the predictions of the ensemble models by integrating the ensemble members based on their performance (Giorgi and Mearns, 2002b). The REA method derives optimal simulations by assigning weights to each model based on their performance in reproducing historical true values and on their convergence in future predictions. The "optimal" integrated ensemble typically performs better than the multi-model ensemble mean or any individual model (Eyring et al., 2019; Flato et al., 2013; Tebaldi and Knutti, 2007).

This study aims to project the global leaf area index (LAI) changes during the 21st century using the optimally integrated CMIP5 and CMIP6 models. To achieve this, we first evaluated the performance of the 16 CMIP5 and 17 CMIP6 models in simulating the global LAI changes with three long-term satellite observed global LAI data sets. Then, we assigned the optimal integration weights to the ESMs based on their performance in simulating the annual LAI changes during the period 1982–2004 and their convergence in simulated LAI changes by the end of the 21st century. We projected the global LAI changes during the 21st century using the CMIP5/6 models with both optimal integration and the traditional multi-model ensemble mean strategies. Lastly, we also analyzed the driving mechanisms of the projected LAI changes based on the optimally integrated ESMs.

2. Methods

2.1. Remote sensing LAI

Remote sensing LAI products can be used to evaluate the performance of the CMIP5/6 ESMs in simulating the dynamics of global vegetation during recent decades (Anav et al., 2013a). We used three long-term remote sensing LAI products, including the Global Inventory Modeling and Mapping Studies third-generation LAI product (GIMMS LAI3g), the Global Land Surface Satellites LAI product (GLASS LAI), and the Global Mapping LAI product (GLOBMAP LAI). The GIMMS LAI3g data was an updated version generated using the latest version (third generation) Advanced Very High Resolution Radiometer (AVHRR), Normalized Difference Vegetation Index (NDVI) data and Moderate-Resolution Imaging Spectroradiometer (MODIS) LAI Collection 6 data based on Artificial Neural Network algorithm (Zhu et al., 2013). The updated GIMMS LAI3g data provides global coverage with 1/12 ° spatial resolution and 15-day temporal resolution from 1982 to 2016. The GLASS LAI data set was derived from AVHRR, MODIS, and CYCLOPES reflectance and LAI products using general regression neural networks (Xiao et al., 2014). We used the latest version of the GLASS LAI data which spans from 1981 to 2017 with 8-day temporal resolution and 1-km spatial resolution. The GLOBMAP LAI was estimated by quantitative fusion of MODIS and historical AVHRR data (Liu et al., 2012). The GLOBMAP LAI is a combination of the AVHRR and MODIS LAI, with global coverage at 15-day temporal resolution and 8-km spatial resolution for the period 1981–2016. We resampled the three LAI products into 1° × 1° spatial resolution grids using the bicubic resampling method, and composited them to monthly temporal resolution based on the maximum value composition method. We then calculated annual mean LAI for the global vegetated grids.

2.2. CMIP5 and CMIP6 Earth system models

We used the historical, Representative Concentration Pathway (RCP) 2.6, RCP4.5 and RCP8.5 simulations by 16 ESMs that have been coordinated by the CMIP5 (Taylor et al., 2012) (https://esgf-node.llnl.gov/search/cmip5/) and the historical, the tier-1 Shared Socioeconomic Pathways (SSPs) SSP1–2.6, SSP2–4.5, SSP3–7.0 and SSP5–8.5 simulations by 17 ESMs that have been coordinated by the latest CMIP6 (Eyring et al., 2016) (https://esgf-node.llnl.gov/search/cmip6/). We selected these models based on their data availability. Table S1 summarizes the CMIP5 and CMIP6 ESMs used in this study. To keep the consistency between the model simulations, we only used the outputs from the first realization (r1i1p1) of all the ESMs. We tried to make full use of the satellite observations and ESMs simulations by using their overlapping time series as long as possible. Note that CMIP5 and CMIP6 provide different end year of the historical simulation (2005 for CMIP5 and 2014 for CMIP6). The monthly output variables, including LAI, surface air temperature, precipitation, surface downwelling shortwave radiation, were downloaded from the CMIP5/6 archives. All the variables were resampled to 1° × 1° spatial resolution. We then calculated the annual mean LAI, annual mean surface air temperature (T), annual total precipitation (P), and annual mean radiation (R) for the global vegetated grids.

2.3. Multi-model ensemble integration strategies

In this study, future changes in LAI refer to the difference in annual mean LAI between the periods of 2078–2100 (future) and 1982–2004 (present-day) for CMIP5 and CMIP6. We projected future global LAI changes and quantified the uncertainties based on the integration of the simulations of CMIP5 and CMIP6 ESMs. For all the model simulations, the annual mean LAI time series of all vegetated grids were subtracted by their present-day average annual mean LAI. For the MME integration, we averaged the annual mean LAI time series of all vegetated grids across the ESMs. The MME LAI time series of all vegetated grids were then weighted by their area and aggregated to regional or global scale.

In addition to the traditional MME method, we also used the REA method to optimally integrate the simulations of all the ESMs. The REA integration strategy assigns different averaging weights to each ESM according to their performance in simulating present-day LAI changes

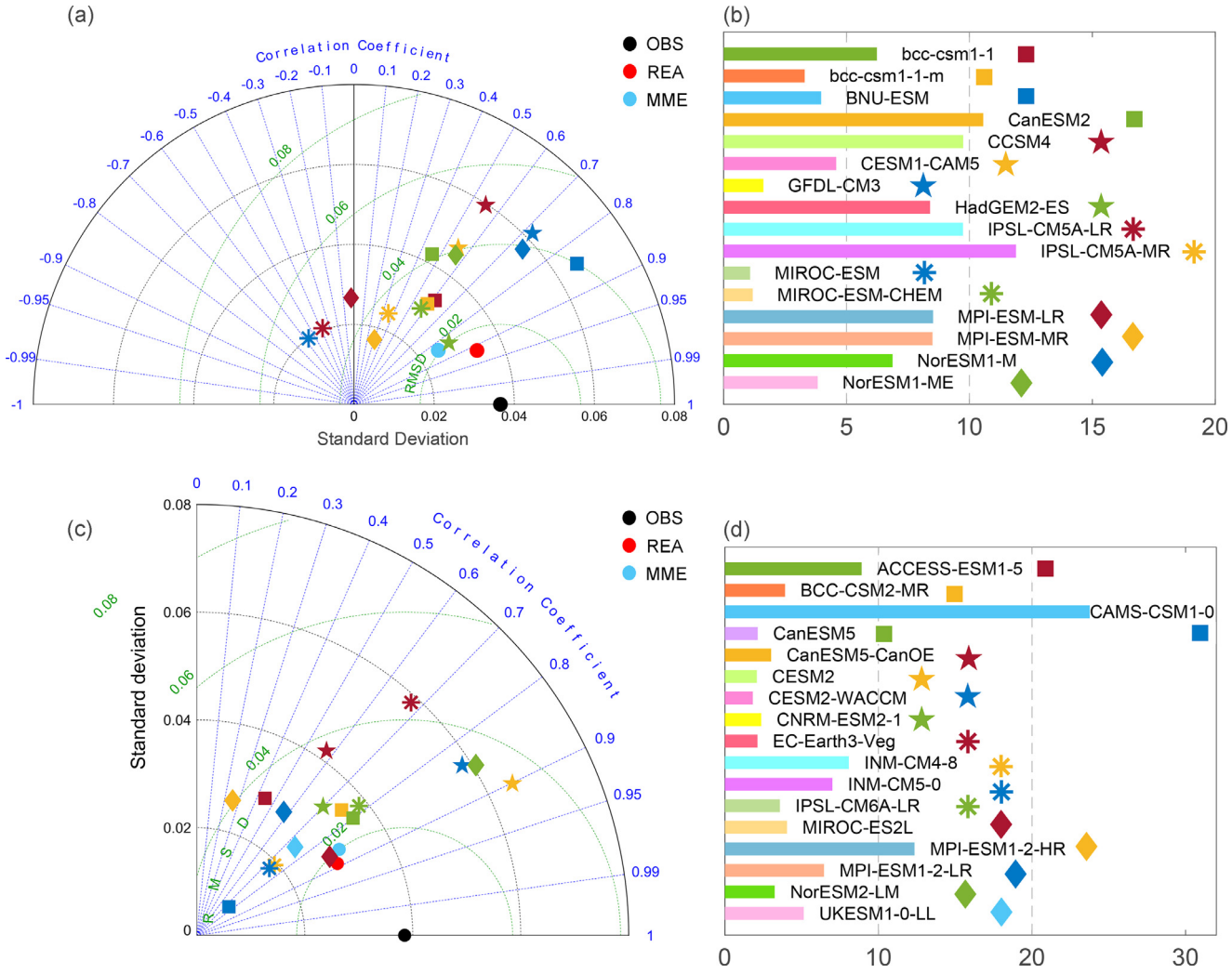

Fig. 1. Evaluation of the performances of the selected ESMs of CMIP5 (a and b) and CMIP6 (c and d). The Taylor diagrams (a and c) compare the remotely-sensed and model-simulated global annual mean LAI for the historical period (1982–2004 for CMIP5, 1982-2014 for CMIP6). The standard deviation shows the interannual variability of the observed and modeled LAI. The dashed green lines show centered root mean square difference (RMSD) between model simulations and satellite observations. (b and d) show the area fractions of the models assigned with the maximum weights. (For interpretation of the references to color in this figure legend, the reader is referred to the web version of this article.)

and convergence in future LAI changes (Giorgi and Mearns, 2002b). In this study, the REA LAI change was calculated as a weighted average of LAI simulated by the ESMs (Giorgi and Mearns, 2002a), that is,

$$\widetilde{\Delta L} = \frac{\sum_{i=1}^{N} R_i \Delta L_i}{\sum_{i=1}^{N} R_i} \quad (1)$$

where ΔL_i is the LAI change simulated by model i, $\widetilde{\Delta L}$ is the LAI change estimated from the REA method, N is the total number of the ESMs, R_i is the reliability factor of model i, which is given by:

$$R_i = [(R_{B,i})^m \times (R_{D,i})^n]^{[1/(m+n)]} \quad (2)$$

$R_{B,\,i}$ is a factor that measures the reliability of model i as a function of the model bias in simulating present-day LAI. The bias is defined as the difference between the simulated and observed LAI. $R_{D,\,i}$ is a factor that measures the degree of convergence of model i with other models. Parameters m and n are weights of $R_{B,\,i}$ and $R_{D,\,i}$, respectively. Specifically, $R_{B,\,i}$ and $R_{D,\,i}$ are given by:

$$\mathrm{R_i} = [(\mathrm{R_{B,i}})^{\mathrm{m}} \times (\mathrm{R_{D,i}})^{\mathrm{n}}]^{[1/(m+n)]} = \left[\left(\frac{d\varepsilon}{\mathrm{B_{L,i}}}\right)^{a} \times (\mathrm{r_{L,i}})^{b} \times \left(\frac{1}{\mathrm{D_{L,i}}}\right)^{c}\right]^{[1/(a+b+c)]} \quad (3)$$

In Eq. (3), $B_{L,\,i}$ is the standard deviation of the distances between the time series of observed and modeled LAI during present-day, $r_{L,\,i}$ is the correlation coefficient of present-day time series between the average of three observed LAI and modeled LAI, and $D_{L,\,i}$ is the distance of a given model from future LAI integrated with the REA weights of the last iteration. $d\varepsilon$ is the natural variation of LAI, which is jointly quantified by the standard deviation of the average time series of the three observed LAI (ε) and the scaling factor (d). a, b, and c are the power of the weighting factors. We tested the robustness of the simulated results by adjusting these powers of the weighting factors and selected the combination of parameters for the following analysis ($a = 1$, $b = 1$, $c = 1$, $d = 0.5$) (Figs. S1-S4).

2.4. Analyzing the effects of environmental factors on future LAI changes

We regressed the simulated interannual LAI time series against the simulated interannual time series of the main driving factors, i.e., atmospheric CO_2 concentration (CO_2), temperature (T), precipitation (P) and surface radiation (R), applying a multiple linear regression model at the pixel level for each individual ESM:

$$LAI_i = \alpha_i\, CO_{2i} + \beta_i\, T_i + \gamma_i\, P_i + \delta_i\, R_i + \varepsilon_i \quad (4)$$

The parameters $\alpha_i, \beta_i, \gamma_i$, and δ_i are the regression coefficients of the main drivers (CO_2, T, P, R) for individual ESM i. ε_i is the residual error. We used the linear regression model (Eq. (4)) to establish the relationship between LAI changes and driving factors in each ESM. For a given driving factor F, we calculated its contribution to future LAI changes as:

$$\Delta F = \left(\sum_{i=1}^{N} R_i \times \Delta F_i\right) / \sum_{i=1}^{N} R_i \quad (5)$$

Here, ΔF_i is determined by multiplying the changes in the driving factor between present-day and future and its corresponding correlation coefficient estimated from Eq. (4). R_i is the REA weight for ESM i estimated from Eq. (3). It should be noted that R_i is equal to 1/N for all ESMs when we perform the attribution analysis based on the MME method.

3. Results

3.1. Evaluation of CMIP5 and CMIP6 ESMs

We evaluated the abilities of CMIP5 and CMIP6 ESMs in simulating present-day global LAI changes by comparing the LAI changes simulated by individual models, MME LAI, and REA LAI to remotely-sensed LAI changes using the Taylor diagram (Taylor, 2001). The performance of the modeled LAI was quantified by the standard deviation (SD) of the modeled and observed interannual LAI time series and their correlation coefficient (r) and the root mean square difference (RMSD) (Fig. 1a, c). As reference, the average of the three remote sensing LAI datasets suggests that the SD of the global annual mean LAI is 0.037. The SD of the CMIP5 ESMs ranges from 0.017 m^2m^{-2} (MPI-ESM-MR) to 0.066 m^2m^{-2} (BNU-ESM), while the SD of the CMIP6 ESMs ranges from 0.008 m^2m^{-2} (CAMS-CSM1–0) to 0.065 m^2m^{-2} (CESM2). The RMSD of CMIP5 ESMs ranges from 0.020 m^2m^{-2} (HadGEM2-ES) to 0.051 m^2m^{-2} (MIROC-ESM), while the RMSD of CMIP6 ESMs ranges from 0.020 m^2m^{-2} (MIROC-ES2L) to 0.043 m^2m^{-2} (EC-Earth3-Veg). It seems that the RMSD between observed LAI and LAI simulated by CMIP6 ESMs (RMSD $<$ 0.040 m^2m^{-2} for 16 out of 17 ESMs) are generally smaller than those between observed LAI and LAI simulated by CMIP5 ESMs (RMSD $>$ 0.040 m^2m^{-2} for about half of the ESMs) (Figs. 1a, c). The correlation coefficients between the LAI time series simulated by the CMIP6 ESMs and the observed LAI time series (ranges from 0.257 (MPI-ESM1–2-HR) to 0.901 (CESM2)) are generally larger than those between the LAI time series simulated by the CMIP5 ESMs and the observed LAI (ranges from -0.567 (MIROC-ESM) to 0.845 (BNU-ESM)) (Figs. 1a, c).

The traditional MME integration method significantly improved the performance of the ESMs in simulating present-day LAI changes. The RMSD between LAI_{MME} (simulated LAI integrated with the MME method) and observed LAI of CMIP5 and CMIP6 ESMs are 0.021 m^2m^{-2} and 0.020 m^2m^{-2} respectively, which are smaller than the RMSD of any individual CMIP5 and CMIP6 ESM. The correlation coefficients between LAI_{MME} and observed LAI of CMIP5 and CMIP6 ESMs are 0.842 and 0.856 respectively, which are generally larger than the r of most individual CMIP5 and CMIP6 ESMs. The SD of LAI_{MME} of CMIP5 and CMIP6 ESMs are also close to the SD of observed LAI (Fig. 1a, c). Compared to the traditional MME integration method, the REA integration method shows even better performance in reproducing present-day LAI changes. The LAI_{REA} (simulated LAI integrated with the REA method) shows lower RMSD (0.015 m^2m^{-2} and 0.018 m^2m^{-2} for CMIP5 and CMIP6, respectively), higher r (0.916 and 0.890 for CMIP5 and CMIP6, respectively) and similar SD (0.034 m^2m^{-2} and 0.029 m^2m^{-2} for CMIP5 and CMIP6, respectively) to the observed LAI (Fig. 1a, c).

The weights assigned by REA were good criteria for model evaluation, i.e., models with higher integration weights generally performed better than those assigned lower weights. Fig. 1(b) and (d) show the area fraction of the CMIP5 and CMIP6 ESMs that were assigned with the highest integration weight. The area fraction of the CMIP5 ESMs has the highest integration weights range from 1.08% (MIROC-ESM) to 11.89% (IPSL-CM5A-MR). CCSM4 shows best performance in the northern latitudes (60~70°N), while CanESM2 and MPI-ESM-MR best captured present-day global LAI changes over many regions in the northern mid-latitudes (Fig. S5a). Other ESMs with the highest integration weights were generally more dispersed (Fig. S5a). The area fraction of the CMIP6 ESMs assigned with the highest integration weights ranges from 2.08% (CESM2) to 23.76% (CAMS-CSM1–0). CAMS-CSM1–0 seems to be the best CMIP6 ESM at simulating present-day LAI in the mid and high latitudes of both Northern Hemisphere and Southern Hemisphere, while UKESM1–0-LL, INM-CM5–0 and INM-CM4–8 perform better in the lower latitudes (Fig. S5b). Other CMIP6 ESMs with the highest REA weights were sparsely distributed (Fig. S5b).

3.2. Projection of the changes in global LAI

We used 16 CMIP5 ESMs under historical, RCP2.6, RCP4.5, and RCP8.5 scenarios and 17 CMIP6 ESMs under historical, SSP1–2.6, SSP2–4.5, SSP3–7.0, and SSP5–8.5 scenarios to predict the changes in global LAI during the 21st century. The CMIP5 ESMs integrated with the traditional MME strategy suggest that the increments of global mean LAI between future (2078–2100) and present-day (1982–2004) are 0.121 ± 0.137 m^2m^{-2}, 0.343 ± 0.237 m^2m^{-2}, 0.422 ± 0.350 m^2m^{-2} under RCP2.6 ($\Delta LAI_{MME}^{RCP2.6}$), RCP4.5($\Delta LAI_{MME}^{RCP4.5}$) and RCP8.5 ($\Delta LAI_{MME}^{RCP8.5}$), respectively, which are equivalent to 7.68% ± 8.75%, 21.79% ± 15.08% and 26.86% ± 22.29% of present-day (1982–2004) global average LAI. The CMIP6 ESMs integrated with the traditional MME method suggest that the increments of global mean LAI between future (2078–2100) and present-day (1982–2004) are 0.185 ± 0.131 m^2m^{-2}, 0.306 ± 0.224 m^2m^{-2}, 0.393 ± 0.313 m^2m^{-2}, and 0.544 ± 0.431 m^2m^{-2} under scenarios SSP1–2.6 ($\Delta LAI_{MME}^{SSP1-2.6}$), SSP2–4.5 ($\Delta LAI_{MME}^{SSP2-4.5}$), SSP3–7.0 ($\Delta LAI_{MME}^{SSP3-7.0}$), and SSP5–8.5 ($\Delta LAI_{MME}^{SSP5-8.5}$), respectively, which are equivalent to 11.80% ± 8.35%, 19.46% ± 14.27%, 25.01% ± 19.91%, and 34.64% ± 27.40% of present-day global average LAI. For both CMIP5 and CMIP6, the magnitudes of LAI increments increase as the forcing levels of the future scenarios increase.

In addition to the traditional MME method, we also aggregated the ESMs with the REA method to provide a more reliable projection of LAI changes. Compared to the MME integration method, the REA integration method generally suggests smaller changes and lower uncertainties in global LAI during the 21st century. The REA integrated CMIP5 ESMs suggest that the global LAI changes are 0.086 ± 0.020 m^2m^{-2}, 0.263 ± 0.040 m^2m^{-2} and 0.320 ± 0.065 m^2m^{-2} under the scenarios RCP2.6, RCP4.5 and RCP8.5, respectively, which are equivalent to 5.47% ± 1.60%, 16.71% ± 3.18% and 20.34% ± 5.18% of present-day global average LAI. The REA integrated CMIP6 ESMs suggest that the global LAI changes are 0.152 ± 0.024 m^2m^{-2}, 0.238 ± 0.041 m^2m^{-2}, 0.301 ± 0.055 m^2m^{-2} and 0.394 ± 0.075 m^2m^{-2} under scenarios SSP1–2.6, SSP2–4.5, SSP3–7.0, and SSP5–8.5, respectively, which are equivalent to 9.69% ± 1.90%, 15.13% ± 3.25%, 19.16% ± 4.41% and 25.05% ± 5.99% of present-day global average LAI. The CMIP6 ESMs estimated a larger magnitude of LAI changes than that estimated by CMIP5 ESMs under the scenarios with the same forcing levels (i.e., RCP2.6 vs. SSP1–2.6 and RCP8.5 vs. SSP5–8.5), independently of whether ESMs were integrated with MME or REA method. Interestingly, CMIP5 and CMIP6 estimated similar magnitudes of LAI change under RCP4.5 and SSP2–4.5 with both the MME and REA integration methods.

Fig. 2(c) shows the evolution pathways of the global mean LAI from 1982 to 2100 simulated by the CMIP5 ESMs integrated with both the MME and REA methods under scenario RCP4.5. Both the REA and MME method suggest that the global mean LAI increases continuously, but

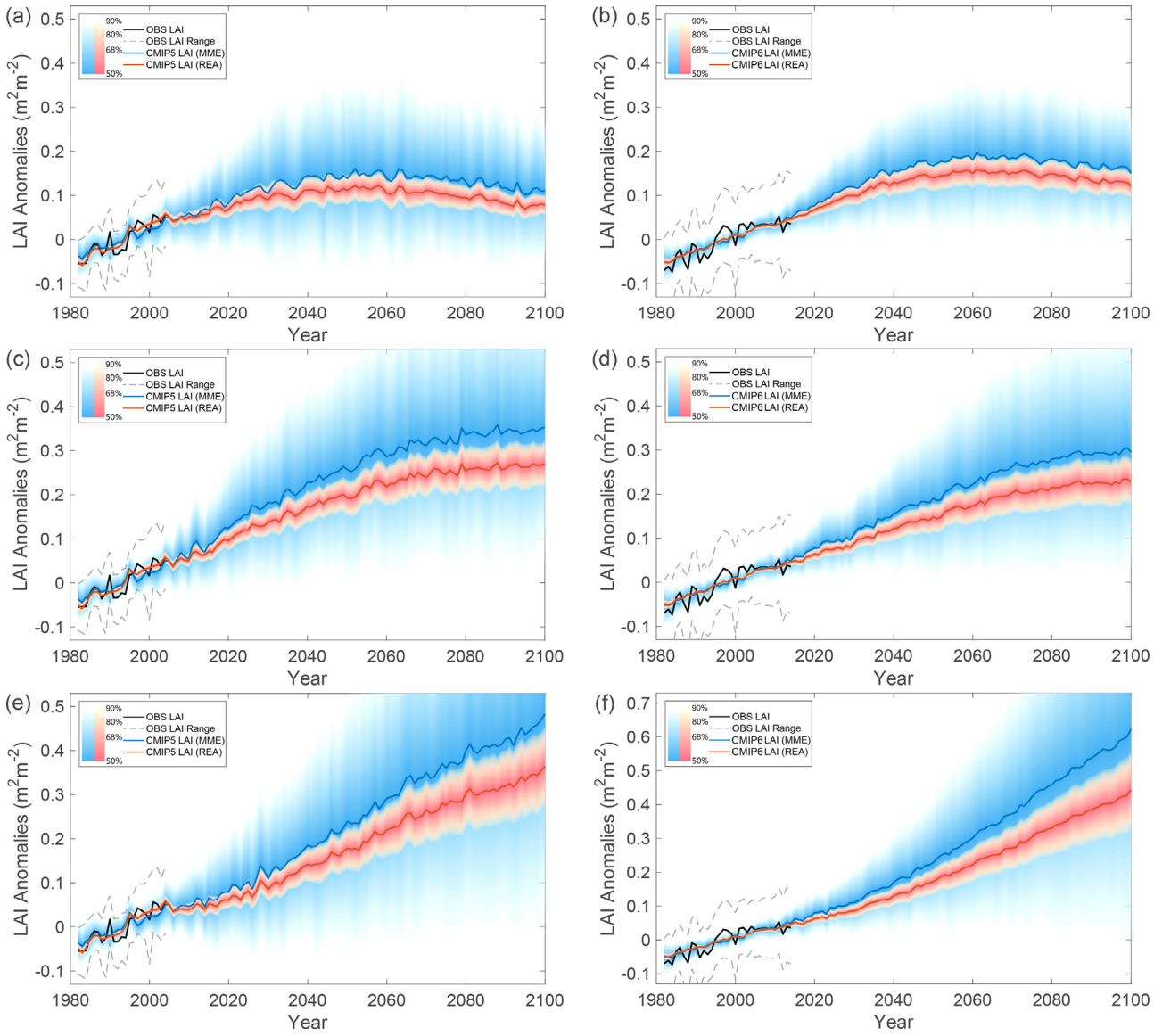

Fig. 2. Interannual changes in global LAI simulated by ESMs integrated with REA (red lines) and MME (blue lines) methods for the period 1982–2100. We estimated the global LAI changes under RCP2.6 (a), SSP1–2.6 (b), RCP4.5 (c), SSP2–4.5 (d), RCP8.5 (e), and SSP5–8.5 (f) scenarios. The average of three satellite-based LAI data (black lines) for the period 1982–2004 (left column) or for the period 1982–2014 (right column), and the range of observed LAI (gray dashed lines). The shaded area shows the uncertainty range of models integrated with the REA (red shading) and MME (blue shading) methods, and the intensity of the shading indicates the distribution probability of the uncertainties. (For interpretation of the references to color in this figure legend, the reader is referred to the web version of this article.)

the increasing rate decreases notably over time. The global LAI changes are more prominent in the northern high latitudes (50~90°N), followed by the equatorial regions and southern high latitudes (50–60°S) (Fig. 3c). Compared to the MME method, the REA method estimated a much lower LAI increment in the northern high latitudes (Fig. 3c). Fig. 4(e) and (g) show the spatial pattern of LAI changes estimated by the CMIP5 ESMs integrated with the MME and REA methods, respectively, under RCP4.5 scenario. The largest ΔLAI_{MME}^{CMIP5} were mainly distributed north of 60°N, followed by Southeast Asia and Central Africa. The negative ΔLAI_{MME}^{CMIP5} were mainly located in Mexico, northern South Africa, and Northern part of South America region (Fig. 4e). The CMIP5 ESMs integrated with REA weights show a much lower magnitude of future LAI changes, but the spatial pattern is similar to that of the ESMs MME (Fig. 4g). For example, the largest ΔLAI_{REA}^{CMIP5} were distributed in similar regions as ΔLAI_{MME}^{CMIP5}, but the magnitude of LAI increment decreases from around 1 m^2m^{-2} to about 0.6 m^2m^{-2} in the northern high latitudes (Fig. 4e, g). The results of the CMIP5 ESMs under other future scenarios integrated with the MME and REA methods are shown in Figs. 2–4. Unlike the CMIP5 ESMs under RCP2.6 and RCP4.5, which showed a decreasing rate of LAI increment, CMIP5 ESMs under RCP8.5 show a strong and constant increasing rate till the end of the 21st century (Fig. 2a, c, e). The spatial patterns of $\Delta LAI_{MME}^{RCP8.5}$ and $\Delta LAI_{REA}^{RCP8.5}$ are similar to those of $\Delta LAI_{MME}^{RCP4.5}$ and $\Delta LAI_{REA}^{RCP4.5}$, but the magnitudes are generally stronger (Fig. 4i, k vs. Fig. 4e, g). Our analysis based on CMIP5 ESMs integrated with MME method show the similar spatial pattern to previous work even if the ESMs used in our study are partly (Mahowald et al., 2016). Interestingly, the spatial patterns of $\Delta LAI_{MME}^{RCP2.6}$ and $\Delta LAI_{REA}^{RCP2.6}$showed pervasive LAI increases in the northern latitudes and widespread decreases in the topics and southern latitudes (Fig. 4a, c).

We also analyzed the trajectory, latitudinal and spatial patterns of future LAI changes based on the latest CMIP6 ESMs under four SSPs. Compared to the results based on the CMIP5 ESMs under the same forcing levels, the CMIP6 projected different increasing rates of global LAI change, and different latitudinal and spatial patterns of LAI changes. Using the REA integration method, the increasing rate of

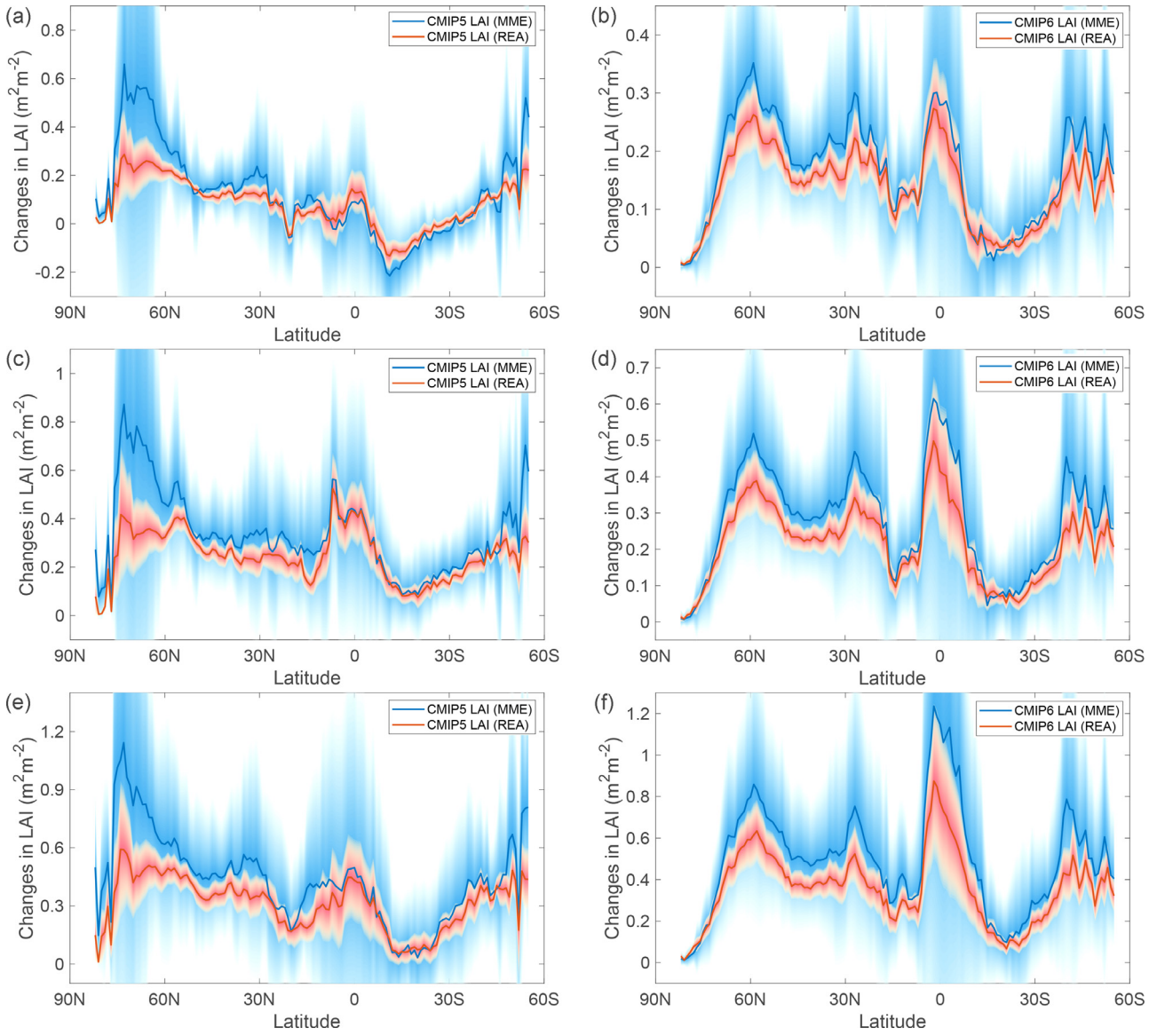

Fig. 3. Latitudinal LAI changes between future (2078–2100) and present-day (1982–2004) simulated by ESMs integrated with REA (red lines) and MME (blue lines) methods. The simulations are under RCP2.6 (a), SSP1–2.6 (b), RCP4.5 (c), SSP2–4.5 (d), RCP8.5 (e), and SSP5–8.5 (f) scenarios. The shaded area indicates the uncertainty range of the models. (For interpretation of the references to color in this figure legend, the reader is referred to the web version of this article.)

global LAI changes projected by the CMIP6 ESMs are 0.0016 $m^2m^{-2}yr^{-1}$, 0.0025 $m^2m^{-2}yr^{-1}$, 0.0031 $m^2m^{-2}yr^{-1}$ and 0.0041 $m^2m^{-2}yr^{-1}$ under SSP1–2.6, SSP2–4.5, SSP3–7.0, and SSP5–8.5 respectively. The latitudinal patterns of future LAI changes projected by CMIP6 ESMs consistently showed that the largest LAI increment is located in the equatorial regions, followed by the northern latitudes (50~70°N), northern mid-latitudes (20~40°N) and southern high latitudes (40–60°S) across all SSPs (Fig. 3b, d, f and S6c). This latitudinal pattern is more similar to the latitudinal pattern simulated by the CMIP5 ESMs integrated with REA weights, which correct the notable high LAI increment in the northern high latitudes according to ΔLAI_{MME}^{RCPs}. The spatial pattern of the LAI changes is also more consistent across different SSPs (although the magnitudes increase as the final forcing level increases). Higher LAI increases are located in the mid northern latitudes, Southeast Asia and central Africa and LAI decreases are found in central and southern Brazil (Fig. 4b, d, f, h, j, l and S6b, d). The spatial patterns of ΔLAI_{MME}^{SSPs} are similar to those of ΔLAI_{REA}^{SSPs}, and the latter show weaker LAI changes (Fig. 4b, f, j and S6b vs. Fig. 4d, h, l and S6d). A notable difference is found between the spatial patterns of LAI changes simulated by CMIP5 ESMs under RCP2.6 and CMIP6 ESMs under SSP1–2.6. Both $\Delta LAI_{MME}^{RCP2.6}$ and $\Delta LAI_{REA}^{RCP2.6}$ suggest that the LAI will decrease in most of the regions in the low and southern latitudes, while $\Delta LAI_{MME}^{SSP1-2.6}$ and $\Delta LAI_{REA}^{SSP1-2.6}$ suggest that the LAI decrements are only notable in central and southern Brazil (Fig. 4a-d).

3.3. Attribution of the global LAI changes

We separated the contributions of the main driving factors, i.e., increasing atmospheric CO_2 concentration ($\Delta LAI_{MME}^{CO_2}$ and $\Delta LAI_{REA}^{CO_2}$), warming (ΔLAI_{MME}^{T} and ΔLAI_{REA}^{T}), and changes in solar radiation ($\Delta LAI_{MME}^{R}$and ΔLAI_{REA}^{R}) and precipitation (ΔLAI_{MME}^{P} and ΔLAI_{REA}^{P}), to future LAI changes between future (2078–2100) and present-day (1982–2004) estimated from both the CMIP5 and CMIP6 ESMs under different scenarios and integrated with both MME and REA (see Methods). Globally, both CMIP5 and CMIP6 ESMs, independently of whether the MME or REA weights were used, suggest that increasing atmospheric CO_2 concentration is the dominant positive driver of future greening of the Earth under all seven scenarios (Fig. 5). The CO_2 fertilization effects were partly canceled out by the effects of global warming on global vegetation. The effects of changes in precipitation

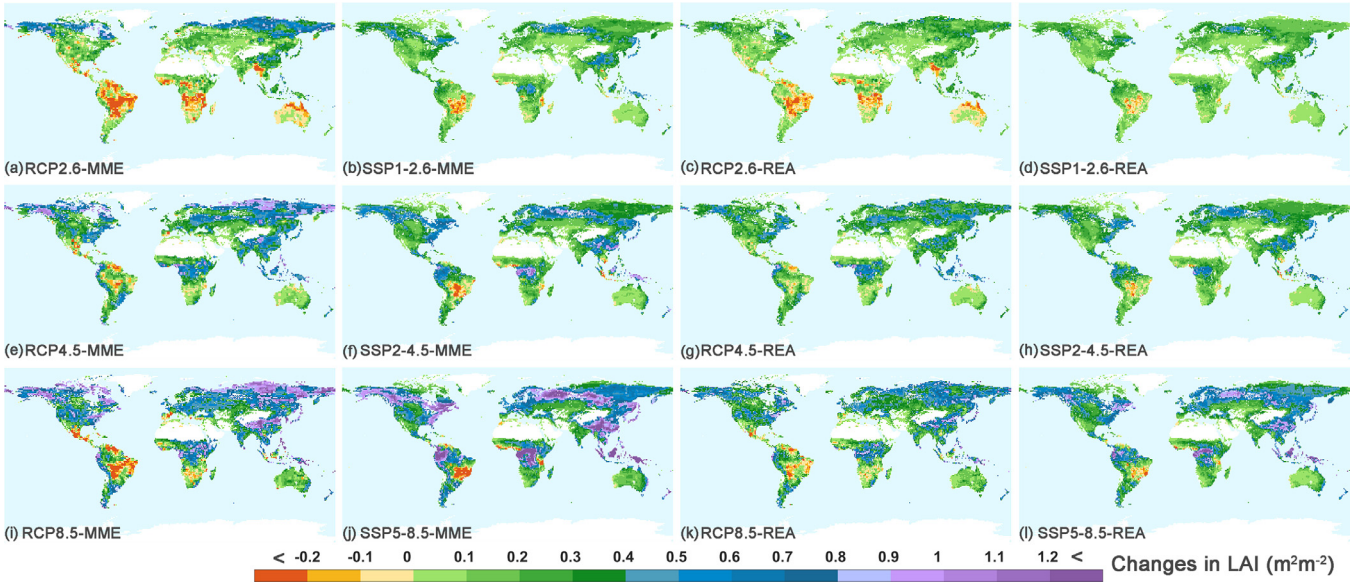

Fig. 4. Spatial patterns of changes in LAI between present-day (1982–2004) and future (2078–2100) estimated by CMIP5 and CMIP6 ESMs. The LAI changes were estimated by the CMIP5 ESMs under RCP2.6, RCP4.5, and RCP8.5 and the CMIP6 ESMs under SSP1–2.6, SSP2–4.5, and SSP5–8.5 integrated with MME and REA methods.

and solar radiation on future global vegetation growth are generally small compared to those of CO_2 fertilization and the warming (Fig. 5 and Tables S3 and S4).

The CMIP6 ESMs indicate notable differences in the contributions of increasing atmospheric CO_2 concentration and global warming to the future greening of the Earth compared to the CMIP5 ESMs. The $\Delta LAI^{CO_2}_{MME}$ of the CMIP5 ESMs is generally larger than that of the CMIP6 ESMs under the same scenarios, and the difference increases as the forcing levels of the scenarios increase. For example, the $\Delta LAI^{CO_2}_{MME}$ of CMIP5 and CMIP6 are 0.262 ± 0.149 m^2m^{-2} and 0.248 ± 0.163 m^2m^{-2} under RCP2.6 and SSP1–2.6 and 0.889 ± 0.454 m^2m^{-2} and 0.616 ± 0.475 m^2m^{-2} under RCP8.5 and SSP5–8.5 (Fig. 5). The differences in the contributions of future global warming between CMIP5 and CMIP6 ESMs are more significant. ΔLAI^{T}_{MME} of CMIP5 are -0.192 ± 0.124 m^2m^{-2}, -0.350 ± 0.226 m^2m^{-2} and -0.532 ± 0.449 m^2m^{-2} under RCP2.6, RCP4.5 and RCP 8.5, while ΔLAI^{T}_{MME} of CMIP6 indicated half the amount of global warming under scenarios of the same forcing levels (-0.090 ± 0.065 m^2m^{-2}, -0.163 ± 0.109 m^2m^{-2} and -0.121 ± 0.123 m^2m^{-2} for SSP1–2.6, SSP2–4.5 and SSP5–8.5, respectively) (SSP3–7.0 see Fig. S7). Given that the contributions of precipitation and radiation changes are much smaller than the contributions of increasing atmospheric CO_2 concentration and warming, which partly resulted from the cancelation of the negative and positive effects of precipitation and solar radiation across different regions (Fig. 6i-p). Interestingly, the $\Delta LAI^{CO_2}_{REA}$ is smaller than $\Delta LAI^{CO_2}_{MME}$ and ΔLAI^{T}_{REA} is less severe than ΔLAI^{T}_{MME} of CMIP5 ESMs under all future scenarios (Fig. 5 and Table S3). It seems that with the REA integration method, the CMIP5 results are closer to the CMIP6 results. However, the REA method also lowers the CO_2 fertilization effect and attenuates the negative warming effect of the CMIP6 ESMs (Fig. 5 and Table S4), indicating that the CMIP6 ESMs may still overestimate the CO_2 fertilization effects and be oversensitive to negative warming effects.

The differences between CMIP5 and CMIP6 in simulating the contributions of the environmental drivers may result from the differences between their projections in future changes in the environmental drivers (Table S5 and Fig. S8) and the differences between their simulations in the sensitivity of LAI to the changes in the environmental drivers. With the traditional MME integration method, LAI changes per 100 ppm CO_2 ($\Delta LAI^{100ppm}_{MME}$) are 0.380 ± 0.212 m^2m^{-2}, 0.363 ± 0.153 m^2m^{-2}, 0.186 ± 0.093 m^2m^{-2} estimated by CMIP5 models under RCP2.6, RCP4.5, and RCP8.5, respectively. CMIP6 ESMs integrated with MME method generally suggest lower $\Delta LAI^{100ppm}_{MME}$ compared to that estimated by CMIP5 models under scenarios with the same forcing levels (0.249 ± 0.160 m^2m^{-2}, 0.190 ± 0.124 m^2m^{-2}, and 0.098 ± 0.074 m^2m^{-2} under SSP1–2.6, SSP2–4.5, and SSP5–8.5, respectively). Both CMIP5 and CMIP6 suggest that $\Delta LAI^{100ppm}_{MME}$ decreases as forcing levels increase (Table S6). We also compared the LAI changes per 100 ppm CO_2 increase estimated by CMIP5 and CMIP6 models that were integrated with the REA method. For both CMIP5 and CMIP6, $\Delta LAI^{100ppm}_{REA}$ was generally lower than $\Delta LAI^{100ppm}_{MME}$ under the same forcing level, and both $\Delta LAI^{100ppm}_{REA}$ and $\Delta LAI^{100ppm}_{REA}$ decreases as forcing levels increase (Table S6).

We also compared the LAI changes per 1 °C temperature increase based on CMIP5 and CMIP6 models with MME and REA integration methods. CMIP5 models integrated with MME method suggest that LAI changes per 1 °C temperature increase ($\Delta LAI^{1^{\circ}C}_{MME}$) are -0.154 ± 0.117 m^2m^{-2}, -0.166 ± 0.116 m^2m^{-2} and -0.125 ± 0.107 m^2m^{-2} under RCP2.6, RCP4.5, and RCP8.5, respectively. CMIP6 models estimated a weaker $\Delta LAI^{1^{\circ}C}_{MME}$ (-0.060 ± 0.038 m^2m^{-2}, -0.060 ± 0.038 m^2m^{-2}, and -0.025 ± 0.030 m^2m^{-2} under SSP1–2.6, SSP2–4.5, and SSP5–8.5, respectively). Both CMIP5 and CMIP6 models that were integrated with REA method estimated more moderate LAI changes per 1 °C temperature increase ($\Delta LAI^{1^{\circ}C}_{REA}$) than that estimated by CMIP5 and CMIP6 models integrated with MME method. The CMIP5 models estimated a stronger $\Delta LAI^{1^{\circ}C}_{REA}$ (-0.100 ± 0.020 m^2m^{-2}, -0.108 ± 0.021 m^2m^{-2}, -0.077 ± 0.020 m^2m^{-2} under RCP2.6, RCP4.5, and RCP8.5, respectively) compared to that were estimated by the CMIP6 models (-0.041 ± 0.008 m^2m^{-2}, -0.040 ± 0.008 m^2m^{-2}, and -0.013 ± 0.006 m^2m^{-2} under SSP1–2.6, SSP2–4.5, and SSP5–8.5, respectively).

The CMIP5 and CMIP6 ESMs show similar spatial patterns of the contributions of the driving factors although their estimation of the magnitudes of the contributions are different (Fig. 6). Generally, the magnitude of the contributions increases with the forcing level of the scenario (Fig. 5). For example, Fig. 6 shows the spatial patterns of the contributions of increasing atmospheric CO_2 concentration, global warming, changes in precipitation and solar radiation to future LAI changes under RCP4.5 and SSP2–4.5. The overall spatial patterns of the CO_2 fertilization effects derived from REA and MME are similar

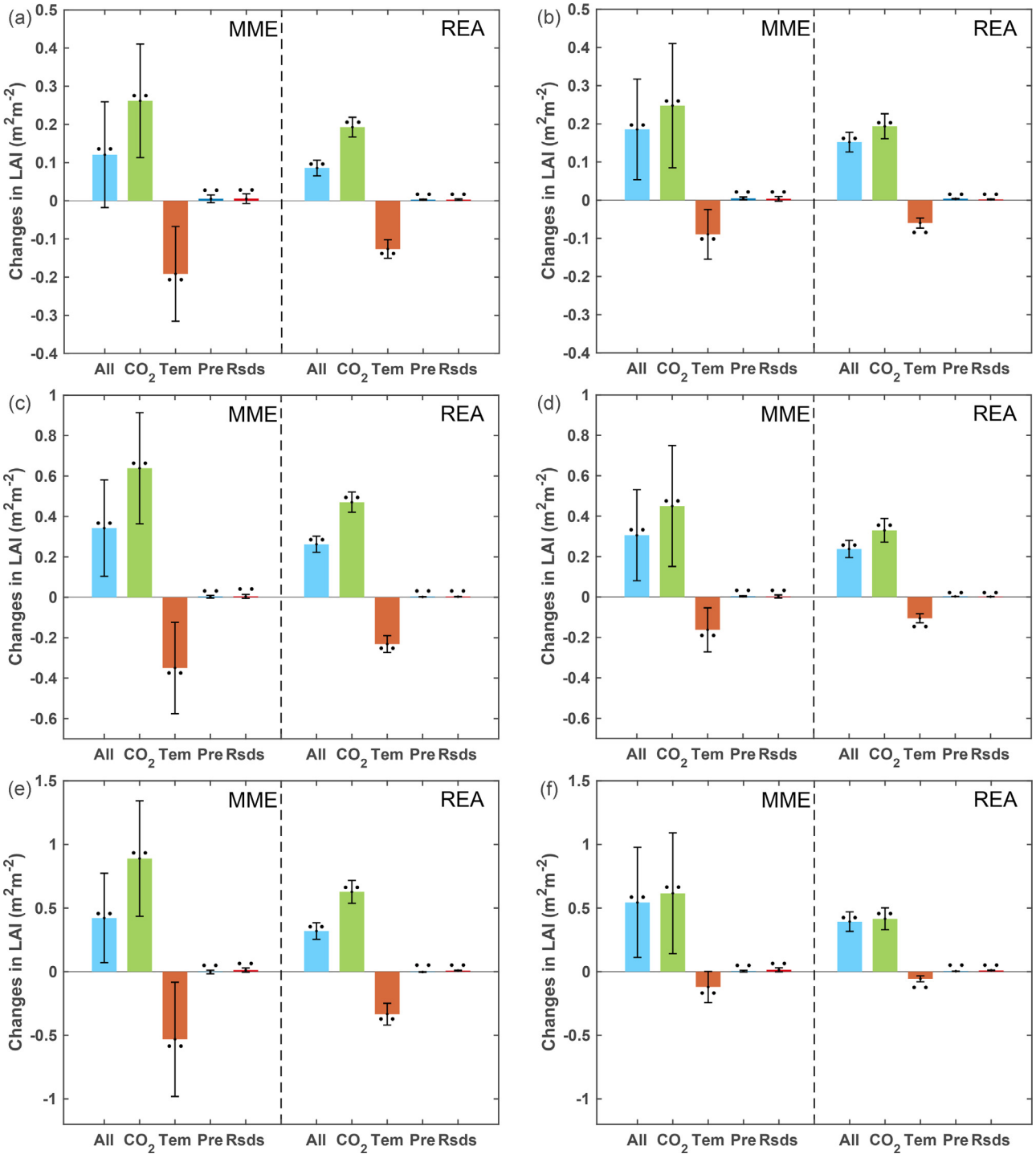

Fig. 5. Contribution of increasing atmospheric CO_2 concentration, surface air temperature, precipitation, and solar radiation to global LAI changes during the 21st century estimated by CMIP5 under scenarios (a) RCP2.6, (c) RCP4.5, (e) RCP8.5, and CMIP6 ESMs under scenarios (b) SSP1–2.6, (d) SSP2–4.5, and (f) SSP5–8.5. In each subfigure, the left panel shows the results estimated from the ESMs integrated with the MME method and the right panel shows the results estimated from the ESMs integrated with REA method. The bars illustrate the standard deviation of the contributions of the environmental factors. Black dots indicate that the contributions are statistically significant ($p < 0.05$).

although $\Delta LAI_{REA}^{CO_2}$ is generally smaller than $\Delta LAI_{MME}^{CO_2}$ across the global vegetated area (Fig. 6a-d). The strongest CO_2 fertilization effects were found in the tropical regions, where more favorable hydrothermal conditions may increase the effects of rising CO_2 concentration on vegetation growth. Rising temperatures stimulated vegetation growth in the northern high latitudes, but also had a much stronger negative effect on the growth of tropical and subtropical vegetation (Fig. 6e-h). Positive precipitation effects were mainly located in central North America, north-central Asia, Northeast China, Amazonia and Central Africa, while negative effects of precipitation were mainly found in western and southern America, Western Europe, Bolivia, Argentina, southern Africa and Australia (Fig. 6i-l). Interestingly, the positive effect of precipitation extends to parts of the croplands in the Northern Hemisphere (Fritz et al., 2015), indicating that precipitation changes are likely to benefit crop production during the 21st century. Solar radiation has notable positive effects on LAI changes during the 21st

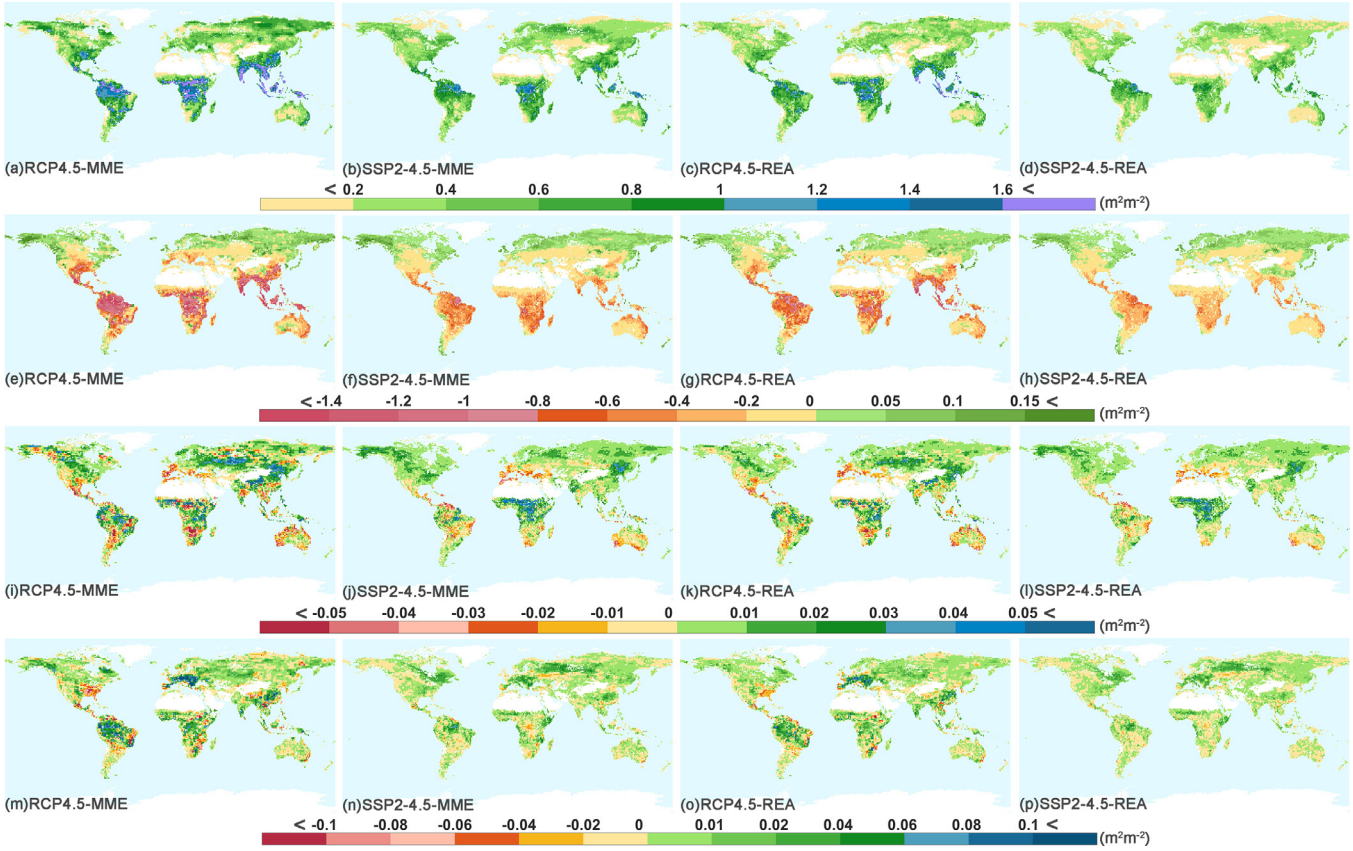

Fig. 6. Spatial patterns of the contribution of increasing atmospheric CO_2 concentration (first row), surface air temperature (second row), precipitation (third row), and solar radiation (last row) to the global LAI changes based on CMIP5 ESMs under RCP4.5 and CMIP6 under SSP2–4.5 during the 21st century integrated with MME and REA methods. Title in each subfigure indicated "Scenario-Method".

century in Western Europe, Southeast Asia, Amazonia, and Central Africa. The negative effects of solar radiation are mainly distributed in east America (Fig. 6m-p). The spatial patterns of the contributions of these driving factors estimated by CMIP5 and CMIP6 ESMs under other future scenarios are shown in Figs. S9–11.

Besides the changes in atmospheric CO_2 concentration, temperature, precipitation, solar radiation, some other factors may also have notable impacts on future global vegetation changes. We further investigated the CMIP5 and CMIP6 ESMs by dividing them into different groups according to their abilities in representing the vegetation dynamics or nitrogen cycling processes (Tables S1 and S2). Generally, the ESMs with vegetation dynamics predict much larger global LAI increments than those without vegetation dynamics. The global LAI changes projected by CMIP5 ESMs with vegetation dynamics under RCP2.6, RCP4.5, and RCP8.5 are 0.163 ± 0.195 m^2m^{-2}, 0.494 ± 0.309 m^2m^{-2} and 0.502 ± 0.505 m^2m^{-2}, respectively. The ESMs without vegetation dynamics simulated much lower LAI increments (0.085 ± 0.071 m^2m^{-2}, 0.226 ± 0.081 m^2m^{-2}, 0.360 ± 0.184 m^2m^{-2}). The CMIP5 ESMs with a vegetation dynamics module predicted much larger LAI increments mainly because they simulated notable LAI increments (>1 m^2m^{-2}) in the northern high latitudes (Fig. 7b, f, j), while the CMIP5 ESMs without vegetation dynamics predicted a magnitude of LAI increment less than 0.2 m^2m^{-2} (Fig. 7a, e, i). It appears that vegetation dynamics is an important process that can affect the projection of global LAI changes. Interestingly, the CMIP5 ESMs integrated with REA agree more with the CMIP5 ESMs without vegetation dynamics in projecting LAI changes in the northern high latitudes, indicating that the vegetation dynamics module of the CMIP5 ESMs may be too sensitive to global environmental changes, which is also found from CMIP6 ESMs. The CMIP6 ESMs with vegetation dynamics also project much larger LAI increments than those without vegetation dynamics (Fig. 7c, g, k vs Fig. 7d, h, l). But they differ in simulating LAI changes in different locations. Taking SSP2–4.5 as an example, their difference was mainly observed in eastern North America, northern high latitudes (60–70°N) of Eurasia, Southeast Asia and Central Africa, where CMIP6 ESMs with vegetation dynamics predicted a much higher LAI increment (>1 m^2m^{-2}) than those without vegetation dynamics (about 0.6 m^2m^{-2}) (Fig. 7g, h and S12f). Also, CMIP6 ESMs with vegetation dynamics predicted that the LAI will decrease by more than −0.2 m^2m^{-2} in Brazil, while the others predicted a minor decrement or even slight increment in LAI. The differences between the CMIP6 ESMs with or without vegetation dynamics under other SSPs are similar (Fig. 7c, d, k, l, S12b, j and S13a, b).

Coupling the nitrogen cycling processes into the ESMs is also a priority task of the modeling community (Goll et al., 2012; Greaver et al., 2016; Liu et al., 2013; Reay et al., 2008; Wang et al., 2017). We divided the CMIP5 and CMIP6 ESMs into different groups according to whether their land model represents the nitrogen cycling processes, and compared their projections of global LAI changes during the 21st century (Fig. 8). The CMIP6 ESMs with nitrogen cycling processes consistently predicted nearly double global LAI increments than those without under all SSPs (Table 1), which is likely due to the fact that ESMs with nitrogen cycling processes considered the nitrogen deposition effects on vegetation growth (Zhu et al., 2017, 2016). However, the CMIP5 ESMs with nitrogen cycling processes predicted similar or even lower global LAI increments than those without (Table 1). This may be because the nitrogen cycling processes in the land models of CMIP5 ESMs are not as good as those in the CMIP6 ESMs, and the nitrogen cycling processes may include a strong nitrogen limitation effect on vegetation growth (Anav et al., 2013a; Huang et al., 2017). Nevertheless, model intercomparison projects that coordinate a factorial set of simulations, i.e., simulations forced by prescribed protocols of

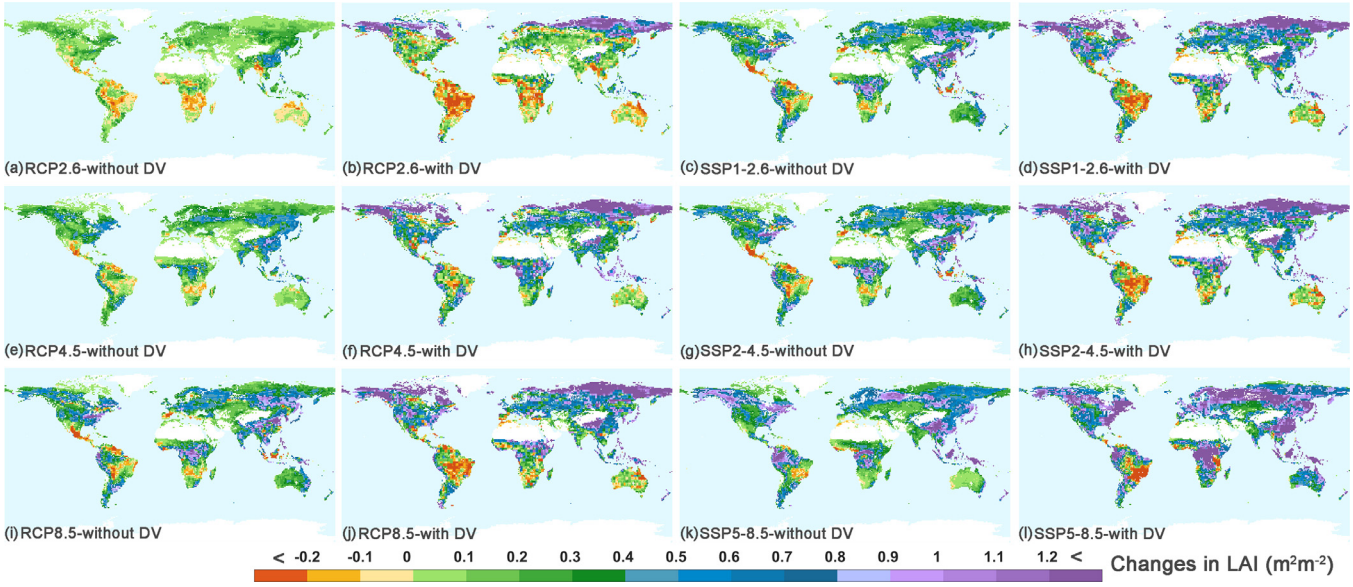

Fig. 7. Spatial patterns of changes in LAI between future (2078–2100) and present-day (1982–2004) simulated by ESMs with or without a dynamic vegetation (DV) module. The first and second columns show the spatial patterns of LAI changes estimated by the CMIP5 ESMs without and with a dynamic vegetation module under RCP2.6, RCP 4.5, and RCP8.5. The third and last columns show the spatial patterns of LAI changes estimated by the CMIP6 ESMs without and with a dynamic vegetation module under SSP1–2.6, SSP2–4.5, and SSP5–8.5. Tables S1 and S2 list the details of the CMIP5 and CMIP6 ESMs representing the dynamic vegetation processes.

varying or constant atmospheric CO_2, climatic variables and other driving factors, will help better understand the driving mechanisms of future global LAI changes (Gillett et al., 2016; O'Neill et al., 2016; Pascoe et al., 2019).

4. Discussion

An increasing number of ESMs are being developed and used in large model inter-comparison projects (Pascoe et al., 2019; Taylor et al., 2012). Model inter-comparison exercises produce an ensemble of simulations by coordinating a group of ESMs forced by common driving data sets and/or same prescribed scenarios (Anav et al., 2013a; Gillett et al., 2016; O'Neill et al., 2016; Pincus et al., 2016; Zanchettin et al., 2016). The MME method has been widely used to integrate simulations of ESMs in these model inter-comparison projects (IPCC, 2013; Mao et al., 2016; Sun et al., 2014; Xu et al., 2019; Zeng et al., 2016). If we regard a model simulation as the combination of signal and noise, the MME method can partially offset the noises and highlight the signals of the model ensemble (Allen and Stott, 2003; Giorgi and Mearns, 2002b; IPCC, 2013; Ribes et al., 2013). But this assumption is not always valid. Another limitation of the MME method is that it treats all the models equally regardless of their performance. This strategy may not reasonably integrate ensembles when models show large systematic discrepancies or differ significantly from the

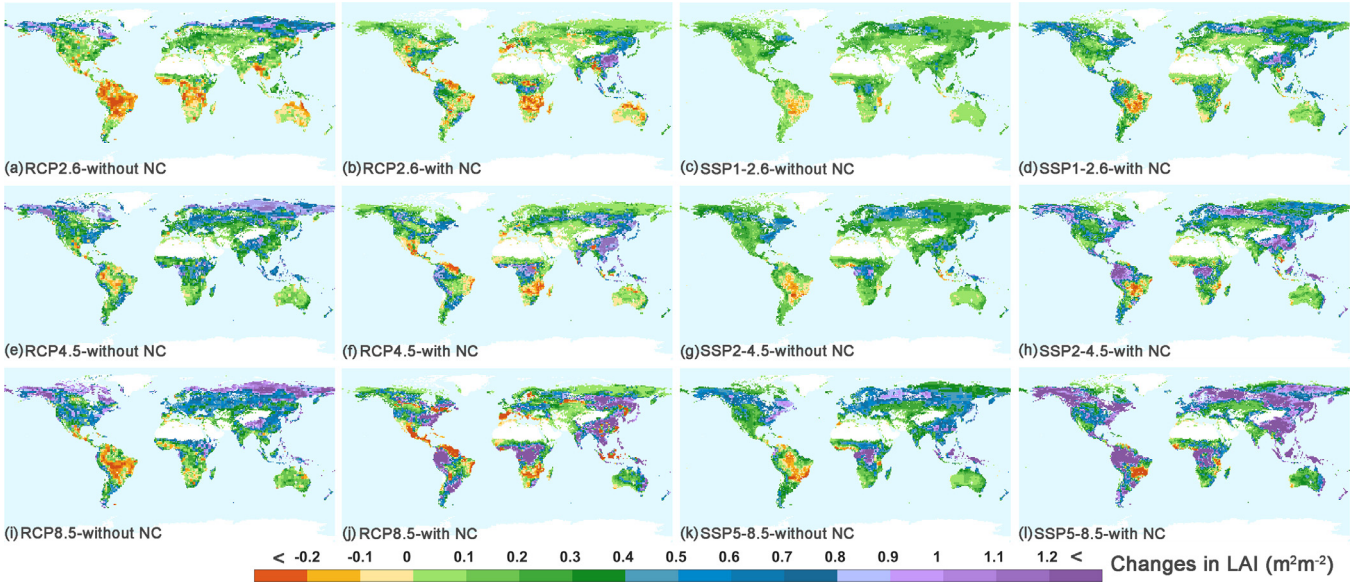

Fig. 8. Spatial patterns of changes in LAI between future (2078–2100) and present-day (1982–2004) simulated by ESMs with or without a nitrogen cycling (NC) module. The first and second columns show the spatial patterns of LAI changes estimated by the CMIP5 ESMs without and with a nitrogen cycling module under RCP2.6, RCP 4.5, and RCP8.5. The third and last columns show the spatial patterns of LAI changes estimated by the CMIP6 ESMs without and with a nitrogen cycling module under SSP1–2.6, SSP2–4.5, and SSP5–8.5. Tables S1 and S2 listed the details of the CMIP5 and CMIP6 ESMs in representing the nitrogen cycling processes.

Table 1
Changes in global mean LAI in the 21st century projected by different groups of CMIP5 and CMIP6 ESMs. The ESMs were classified into four groups according to the abilities of their land model in simulating nitrogen cycling (NC) and vegetation dynamics (VD). A full list of CMIP5 and CMIP6 ESMs and whether their land models include the ability to simulate NC or VD processes are listed in Tables S1 and S2.

CMIP phase	Scenario	NC on	NC off	VD on	VD off
CMIP5 (m^2m^{-2})	RCP2.6	0.139 ± 0.071	0.109 ± 0.155	0.163 ± 0.195	0.085 ± 0.071
	RCP4.5	0.278 ± 0.059	0.357 ± 0.273	0.494 ± 0.309	0.226 ± 0.081
	RCP8.5	0.454 ± 0.084	0.402 ± 0.405	0.502 ± 0.505	0.360 ± 0.184
CMIP6 (m^2m^{-2})	SSP1–2.6	0.251 ± 0.142	0.139 ± 0.107	0.242 ± 0.083	0.168 ± 0.141
	SSP2–4.5	0.422 ± 0.231	0.224 ± 0.189	0.424 ± 0.156	0.269 ± 0.234
	SSP3–7.0	0.545 ± 0.342	0.286 ± 0.255	0.559 ± 0.239	0.341 ± 0.322
	SSP5–8.5	0.756 ± 0.462	0.395 ± 0.356	0.792 ± 0.320	0.467 ± 0.440

observations. For example, the CMIP5 ESMs show large discrepancies in global LAI changes during the 21st century (Fig. S14). Several models simulate a much higher increase in global LAI, while a majority simulates a relative lower LAI increment (Fig. S14). As a result, by averaging all the models without considering their performance, the traditional MME method estimated a relatively high LAI increase.

These problems can be partly solved by the REA method because it assigns integration weights to the models according to their performance (Giorgi and Mearns, 2002b). A model that shows large bias compared to the reference data is assigned low weights for the integration. This strategy not only minimizes the contribution of these simulations to the ensembles, but also reduces the uncertainties of the integration. However, while the REA method is helpful for the integration of the multi-model simulations, it cannot overcome the problems inherent in the models. According to our analyses, current ESMs show notable biases in simulating global LAI compared to satellite observations (Fig. S14). A number of factors can explain the uncertainties in the ESMs. Deficiencies in the parameterization and structure of the ESMs modules, coupling strategies among the modules, uncertainties in the driving data sets all contribute to biases in the simulation outputs (Anav et al., 2013a; IPCC, 2013). The REA method cannot help improve the performance of any individual ESM. Further refinements of ESMs are still the fundamental for improving simulations of global LAI changes. The first priority is to improve the performance of ecosystem models, i.e., the land module of ESMs. The parameterization and representation of the processes of phenology, allocation, nutrients cycling, wetlands and peatlands, forest establishments and mortality, and natural disturbances in current ecosystem models are still quite poor (Anav et al., 2013a, 2013b; Huang et al., 2017; Mao et al., 2016; Murray-Tortarolo et al., 2013; Zhu et al., 2016). Fortunately, the models are developing and some of them (e.g., CLM4.5) have shown significant improvements compared to their previous versions (Peano et al., 2019). More importantly, the mechanisms of response and adaptation of vegetation to global environmental change, which is very important for projecting future LAI changes, are still not clear. An ESM not only simulates the land ecosystem independently, it is also coupled with many mechanisms of other components (IPCC, 2013; Pascoe et al., 2019; Taylor et al., 2012). Therefore, the performances of other modules, e.g., atmospheric circulation and radiation, chemistry, sea ice, ocean ecology and biogeochemistry, ocean circulation, plant ecology and land use, land physics and hydrology, and continental ice sheets modules all contribute to the accuracy of global LAI changes simulations. It should be noted that the quality of the reference data, i.e., the remote sensing LAI data, also can affect the reliability of the REA weights. Although the three remote sensing LAI data have been extensively validated against field measurements and other satellite products, we should be aware of their uncertainties and discrepancies (Jiang et al., 2017). Different data sources and retrieval algorithms are the main reasons for the discrepancies between the three LAI data sets (Fang et al., 2013). Furthermore, the inherent caveats of the legacy AVHRR sensors, e.g., lacking of on-board calibration and orbital loss problem, contribute to the uncertainties in the three LAI products (Jiang et al., 2017). Nevertheless, we used three widely-used and irreplaceable satellite products in our analysis, trying to provide more robust reference data for the ESMs.

The reliability of the projection of future global vegetation LAI changes is also affected by the rationality of the prescribed future scenarios. We project the changes in global vegetation LAI based on 16 CMIP5 and 17 CMIP6 ESMs that were optimally integrated using REA strategy under 7 future scenarios during the 21st century. The CMIP5 and CMIP6 ESMs consistently suggest that global LAI will increase under all scenarios (Fig. 2). They also consistently predict that the magnitude of the global LAI increase is proportional to the forcing levels of the future scenarios (Fig. 2). However, the CMIP5 and CMIP6 ESMs still show notable differences in predicting future global LAI, especially at the regional scales (Fig. 4). This discrepancy is mainly resulting from the major differences between the CMIP5 and CMIP6 ESMs. The CMIP6 LAI projections differ from those of CMIP5 because they include a new generation of ESMs, different start year for future scenarios, and a new set of future scenarios (O'Neill et al., 2016). As shown in Tables S1 and S2, the CMIP6 ESMs are new or updated compared to the CMIP5 ESMs. The prevailing hypothesis is that the newer ESMs are improved because the ones used in CMIP5 have been extensively evaluated and their defects have been partly corrected accordingly (Anav et al., 2013a; Pascoe et al., 2019; Stouffer et al., 2017; Taylor et al., 2012). For example, the version of Community Land Model (CLM) used in some CMIP5 ESMs has been updated to CLM5 for the CMIP6 ESMs (Tables S1 and S2), which includes updates in major components, especially in soil and plant hydrology, snow density, river modeling, carbon and nitrogen cycling and coupling, and crop modeling (Lawrence et al., 2019). These improvements are closely related to the performance of the LAI simulation of land models. Another notable difference between CMIP5 and CMIP6 is the end year of the historical simulations and/or the start year of the future scenarios (2005 for CMIP5 and 2015 for CMIP6). This difference will affect the REA method used in this study because of the different number of years in the historical simulation. The last major factor that could cause differences in LAI projections between the CMIP5 and CMIP6 is the difference in future scenarios. The future scenarios of CMIP6 are generally more advanced than those of the CMIP5 in terms of new emissions and land use data, new natural forcing (e.g., solar forcing and volcanic emissions), and the updated versions of integrated assessment models (O'Neill et al., 2016). It is generally believed that different scenarios with the same global forcing pathways are likely to produce similar climate conditions. However, this may not be the case for projecting future LAI. For example, the CO_2 concentration, a key driving factor for global LAI, of SSP5–8.5 is different from that of RCP8.5 (O'Neill et al., 2016; Riahi et al., 2017). Land use change also differs between SSP5–8.5 and the previous RCP8.5. We recognize that the uncertainty analysis of LAI projections between the CMIP5 and CMIP6 could be problematic, as the separation of model and scenario uncertainty is unclear (Knutti and Sedlacek, 2013; O'Neill et al., 2016). Nevertheless, the RCPs-based projections with CMIP5 ESMs could be used as valuable

complements of the CMIP6 projections.

Vegetation is highly sensitive to global environmental changes (Huang et al., 2019; Zhu et al., 2016). Our study showed that global vegetation is expected to change significantly during the 21st century under the scenarios that the global environment will continue to be affected by anthropogenic activities. On the other hand, vegetation changes also play important roles in regulating local and global environments (Bonan, 2008). The feedbacks of vegetation include mediating carbon cycling, surface energy balance, and water cycling (Bonan, 2008). Therefore, projected changes in global LAI may have a profound impact on the Earth system in various aspects.

Future changes in global vegetation are expected to strongly impact carbon cycling (IPCC, 2013; Le Quere et al., 2018; Sitch et al., 2015b). LAI is an important canopy parameter that is strongly correlated with photosynthesis and carbon sink capacity of terrestrial ecosystem (Li et al., 2018a; Sellers, 1985; Sellers et al., 1992; Sitch et al., 2015a). In the long-term, our projected large LAI increase of global vegetation may indicate that the photosynthesis and carbon sink capacities of global terrestrial ecosystems will also increase. The enhancement of photosynthesis capacity of future terrestrial ecosystem may result from both gradual LAI increases of a given vegetation type and LAI increase due to changes in vegetation type. For example, woody encroachment is likely pervasive across the whole globe (Huang et al., 2017; Stevens et al., 2017; Van Auken, 2009). This process is supposed to notably increase LAI, as shown in our study (Fig. 7), which further results in an enhancement of photosynthesis capacity. LAI increases due to anthropogenic vegetation type change, e.g., afforestation, forest regrowth after cropland abandonment or deforestation, are also accompanied by increments in photosynthetic capacity and carbon sequestration (Chen et al., 2019; Mueller et al., 2014; Pan et al., 2011; Piao et al., 2018). It should be noted that the relationships between LAI, environmental factors and photosynthetic capacity are complicated. Environmental factors to some extent drive LAI changes and, jointly, determine the photosynthetic capacity of vegetation. Higher atmospheric CO_2 concentration, warmer temperature, together with increasing LAI due to woody encroachment are positive drivers of photosynthesis in the northern latitudes. However, soil moisture and nutrients limitations could to, some extent, offset these positive effects (Huang et al., 2017; Reich et al., 2014; Wang et al., 2014). In addition to the dominant global LAI increment, we should note that there are also some regions showing LAI decreases (Fig. 4). Nevertheless, the dominant global LAI increment during the 21st century is likely to help land carbon sequestration, although our optimal predictions imply that the magnitude may be much lower than previously estimated.

Changes in global LAI are also supposed to have profound impacts on the surface energy budget of the Earth system through direct and indirect physical and biogeochemical processes (Zeng et al., 2017). Increases in LAI generally mean decreases in albedo, resulting in surface warming because more solar radiation will be absorbed by the land surface (Bonan, 2008), a phenomenon called albedo warming. However, albedo warming effects could be offset by the cooling effects of the concomitant increasing evapotranspiration (ET) (Bonan, 2008; Zeng et al., 2017). Our study projects that the LAI of tropical vegetation will increase by 0.4–0.5 m^2m^{-2} during the 21st century. The LAI of tropical vegetation is generally large and its projected increase will not lead to a notable albedo warming according to the radiative transfer theory (Sellers, 1985). Recent studies generally suggest that the ET cooling effects are usually larger than the albedo warming effects in the low latitudes (Bonan, 2008). Thus, the projected LAI increment of tropical vegetation is likely to lead to a net cooling effect resulting from notable ET cooling and slight albedo warming. However, the relative magnitudes of the ET cooling and albedo warming resulting from the LAI increment in the northern latitudes during recent decades is still under debate. Studies based on field experiments suggest that the albedo warming is greater than the ET cooling effect (Betts, 2000; Bonan, 2008; Feddema et al., 2005), while ESM-based studies support the opposite conclusion (Zeng et al., 2017). Both these results provide valuable insights for the consequences of the projected LAI changes in this study. Because the projected LAI changes are resulting from processes including both gradual LAI changes of current vegetation (more like ESM-based studies) and LAI changes due to composition changes or even vegetation type shifts (more like field-based studies). This further complicates the inferences of the relative magnitude of albedo warming and ET cooling due to the projected LAI increments in the northern latitudes. More sophisticated field experiments, e.g., gradual vegetation type change experiments, and improved modeling studies that can well represent processes of ecosystem evolutions are needed to help predict the feedbacks of future LAI changes.

The influence of LAI changes on carbon cycling and the surface energy budget also accompany many other processes that can affect water cycling at regional or global scales (Piao et al., 2019). For example, the ET increase due to LAI increase not only affects the energy budget but also potentially changes the water cycling of terrestrial ecosystems (Bonan, 2008). The ET increase will extract more water from the land to the atmosphere, which is likely associated with more local or remote precipitation (Li et al., 2018b; van der Ent et al., 2010). However, the increasing ET due to LAI increment may also cause a decrease in soil moisture if the balance of water cycling is broken by increasing ET and insufficient water supply (Bonan, 2008; Lian et al., 2020; Zeng et al., 2018). These processes are usually coupled with atmospheric circulation, which is also affected by vegetation surface characteristics (Vautard et al., 2010; Zeng et al., 2017). Through atmospheric circulation, the changes in water cycling due to vegetation changes may have effects on remote regions (Lian et al., 2020).

In summary, we projected the changes in global LAI during the 21st century using the simulations by 16 CMIP5 ESMs under three future scenarios (RCP2.6, RCP4.5 and RCP8.5) and 17 CMIP6 ESMs under four future scenarios (SSP1–2.6, SSP2–4.5, SSP3–7.0 and SSP5–8.5). In addition to the traditional MME method, we also used the REA strategy to integrate the simulations of these ESMs. We assigned integrating weights to these ESMs based on their performance on reproducing present-day global LAI changes observed by satellites and the convergence of future predictions. The ESMs integrated by MME methods and REA weights both suggest that the global LAI will increase under all prescribed future scenarios, and the magnitude of these increments will increase with the forcing levels of future scenarios. However, the ESMs integrated with the REA weights predicted a much lower (19∼29%) LAI increment than those aggregated with the traditional MME method. ESMs integrated with REA weights also significantly reduced the uncertainties of the projected changes in LAI. We also tentatively analyzed the contributions of the changes in atmospheric CO_2 concentration and climate (temperature, precipitation and solar radiation) to the predicted global vegetation LAI changes during the 21st century. The ESMs assigned with REA weights suggest a lower CO_2 fertilization effect and a weaker negative warming effect compared to the MME ESMs, while the contributions of precipitation and radiation changes are generally small and have less discrepancies between the REA and MME methods. Our improved comprehensive projection of future global LAI based on CMIP5 and CMIP6 ESMs and the REA integration strategy are supposed to have broad impacts on the Earth system that are closely related to human society. Although our study somewhat reduced the uncertainties in current ESMs, more research focused on improving the inherent structure and parameterization of ESMs and future scenarios is needed to more reliably project global vegetation changes.

Declaration of Competing Interest

The authors declare that they have no known competing financial interests or personal relationships that could have appeared to influence the work reported in this paper.

Acknowledgments

This work was funded by the National Natural Science Foundation of China (41901122). We thank the World Climate Research Programme's Working Group on Coupled Modeling for organizing CMIP, and we acknowledge the climate modeling groups of CMIP5 and CMIP6 for making their model outputs available. We also acknowledge the people and institutions who provided the remote sensing LAI datasets used in this paper (GLASS LAI and GLOBMAP LAI).

Supplementary materials

Supplementary material associated with this article can be found, in the online version, at doi:10.1016/j.agrformet.2020.108111.

References

Allen, M.R., Stott, P.A., 2003. Estimating signal amplitudes in optimal fingerprinting, part I: theory. Clim. Dyn. 21 (5–6), 477–491. https://doi.org/10.1007/s00382-003-0313-9.

Anav, A., et al., 2013a. Evaluating the land and ocean components of the global carbon cycle in the CMIP5 earth system models. J. Clim. 26 (18), 6801–6843. https://doi.org/10.1175/jcli-d-12-00417.1.

Anav, A., et al., 2013b. Evaluation of land surface models in reproducing satellite derived leaf area index over the high-latitude Northern Hemisphere. Part II: Earth System Models. Remote Sens. 5 (8), 3637–3661. https://doi.org/10.3390/rs5083637.

Beer, C., et al., 2010. Terrestrial gross carbon dioxide uptake: global distribution and covariation with climate. Science 329 (5993), 834–838 https://doi.org/10.1126/science.1184984.

Betts, R.A., 2000. Offset of the potential carbon sink from boreal forestation by decreases in surface albedo. Nature 408 (6809), 187–190.

Bonan, G.B., 2008. Forests and climate change: forcings, feedbacks, and the climate benefits of forests. Science 320 (5882), 1444–1449 https://doi.org/10.1126/science.1155121.

Chen, C., et al., 2019. China and India lead in greening of the world through land-use management. Nat. Sustain. 2 (2), 122–129 https://doi.org/10.1038/s41893-019-0220-7.

Eyring, V., et al., 2016. Overview of the coupled model intercomparison project phase 6 (CMIP6) experimental design and organization. Geosci. Model Dev. 9 (5), 1937–1958 https://doi.org/10.5194/gmd-9-1937-2016.

Eyring, V., et al., 2019. Taking climate model evaluation to the next level. Nat. Clim. Chang. 9 (2), 102–110 https://doi.org/10.1038/s41558-018-0355-y.

Fang, H., et al., 2013. Characterization and intercomparison of global moderate resolution leaf area index (LAI) products: analysis of climatologies and theoretical uncertainties. J. Geophys. Res. 118 (2), 529–548 https://doi.org/10.1002/jgrg.20051.

Feddema, J.J., et al., 2005. The importance of land-cover change in simulating future climates. Science 310 (5754), 1674–1678 https://doi.org/10.1126/science.1118160.

Flato, G., et al., 2013. Evaluation of climate models. In: Stocker, T.F. (Ed.), Climate Change 2013: The Physical Science Basis. Contribution of Working Group I to the Fifth Assessment Report of the Intergovernmental Panel On Climate Change. Cambridge University Press, Cambridge, United Kingdom and New York, NY, USA, pp. 741–866.

Foley, J.A., et al., 2005. Global consequences of land use. Science 309 (5734), 570–574 https://doi.org/10.1126/science.1111772.

Fritz, S., et al., 2015. Mapping global cropland and field size. Glob. Chang. Biol. 21 (5), 1980–1992 https://doi.org/10.1111/gcb.12838.

Gillett, N.P., et al., 2016. The detection and attribution model intercomparison project (DAMIP v1.0) contribution to CMIP6. Geosci. Model Dev. 9 (10), 3685–3697 https://doi.org/10.5194/gmd-9-3685-2016.

Giorgi, F., Mearns, L.O., 2002a. Calculation of average, uncertainty range, and reliability of regional climate changes from AOGCM simulations via the "reliability ensemble averaging" (REA) method. J. Clim. 15 (10), 1141–1158 https://doi.org/10.1175/1520-0442(2002)015<1141:Coaura>2.0.Co;2.

Giorgi, F., Mearns, L.O., 2002b. Calculation of average, uncertainty range, and reliability of regional climate changes from AOGCM simulations via the "reliability ensemble averaging" (REA) method. J. Clim. 15 (10), 1141–1158 https://doi.org/10.1175/1520-0442(2002)015<1141:COAURA>2.0.CO;2.

Goll, D.S., et al., 2012. Nutrient limitation reduces land carbon uptake in simulations with a model of combined carbon, nitrogen and phosphorus cycling. Biogeosciences 9 (9), 3547–3569 https://doi.org/DOI 10.5194/bg-9-3547-2012.

Greaver, T.L., et al., 2016. Key ecological responses to nitrogen are altered by climate change. Nat. Clim. Chang. 6 (9), 836 https://doi.org/10.1038/nclimate3088.

Hovenden, M.J., et al., 2019. Globally consistent influences of seasonal precipitation limit grassland biomass response to elevated CO2. Nat. Plants 5 (2) 167-+. https://doi.org/10.1038/s41477-018-0356-x.

Huang, M., et al., 2019. Air temperature optima of vegetation productivity across global biomes. Nat. Ecol. Evol. 3 (5), 772–779 https://doi.org/10.1038/s41559-019-0838-x.

Huang, M., et al., 2017. Velocity of change in vegetation productivity over northern high latitudes. Nat. Ecol. Evol. 1 (11), 1649–1654 https://doi.org/10.1038/s41559-017-0328-y.

IPCC, 2013. Climate change 2013: the physical science basis. Contribution of Working Group I to the Fifth Assessment Report of the Intergovernmental Panel On Climate Change. Cambridge University Press, Cambridge, United Kingdom and New York, NY, USA, pp. 1535.

Jiang, C., et al., 2017. Inconsistencies of interannual variability and trends in long-term satellite leaf area index products. Glob. Chang. Biol. 23 (10), 4133–4146 https://doi.org/10.1111/gcb.13787.

Jung, M., et al., 2017. Compensatory water effects link yearly global land CO2 sink changes to temperature. Nature 541 (7638), 516–520. https://doi.org/10.1038/nature20780.

Knutti, R., Sedlacek, J., 2013. Robustness and uncertainties in the new CMIP5 climate model projections. Nat. Clim. Chang. 3 (4), 369–373 https://doi.org/10.1038/Nclimate1716.

Lawrence, D.M., et al., 2019. The community land model version 5: description of new features, benchmarking, and impact of forcing uncertainty. J. Adv. Model. Earth Syst. 11 (12), 4245–4287 https://doi.org/10.1029/2018ms001583.

Le Quere, C., et al., 2018. Global carbon budget 2018. Earth Syst. Sci. Data 10 (4), 2141–2194 https://doi.org/10.5194/essd-10-2141-2018.

Li, W., et al., 2018a. Recent changes in global photosynthesis and terrestrial ecosystem respiration constrained from multiple observations. Geophys. Res. Lett. 45 (2), 1058–1068 https://doi.org/10.1002/2017 gl076622.

Li, Y., et al., 2018b. Divergent hydrological response to large-scale afforestation and vegetation greening in China. Sci. Adv. 4 (5) eaar4182. https://doi.org/10.1126/sciadv.aar4182.

Lian, X., et al., 2020. Summer soil drying exacerbated by earlier spring greening of northern vegetation. Sci. Adv. 6 (1) eaax0255. https://doi.org/10.1126/sciadv.aax0255.

Liu, X.J., et al., 2013. Enhanced nitrogen deposition over China. Nature 494 (7438), 459–462 https://doi.org/10.1038/nature11917.

Liu, Y., Liu, R., Chen, J.M., 2012. Retrospective retrieval of long-term consistent global leaf area index (1981-2011) from combined AVHRR and MODIS data. J. Geophys. Res.-Biogeosci. 117 https://doi.org/10.1029/2012jg002084.

Los, S.O., 2013. Analysis of trends in fused AVHRR and MODIS NDVI data for 1982-2006: indication for a CO2 fertilization effect in global vegetation. Global Biogeochem. Cycles 27 (2), 318–330 https://doi.org/10.1002/gbc.20027.

Lucht, W., et al., 2002. Climatic control of the high-latitude vegetation greening trend and Pinatubo effect. Science 296 (5573), 1687–1689 https://doi.org/10.1126/science.1071828.

Mahowald, N., et al., 2016. Projections of leaf area index in earth system models. Earth Syst. Dyn. 7 (1), 211–229 https://doi.org/10.5194/esd-7-211-2016.

Mao, J., et al., 2016. Human-induced greening of the northern extratropical land surface. Nat. Clim. Chang. 6 (10), 959–963 https://doi.org/10.1038/nclimate3056.

Mao, J.F., et al., 2013. Global latitudinal-asymmetric vegetation growth trends and their driving mechanisms: 1982-2009. Remote Sens. (Basel) 5 (3), 1484–1497 https://doi.org/10.3390/rs5031484.

Mueller, T., et al., 2014. Human land-use practices lead to global long-term increases in photosynthetic capacity. Remote Sens. (Basel) 6 (6), 5717–5731 https://doi.org/10.3390/rs6065717.

Murray-Tortarolo, G., et al., 2013. Evaluation of land surface models in reproducing satellite-derived LAI over the high-latitude Northern Hemisphere. Part I: Uncoupled DGVMs. Remote Sens. 5 (10), 4819–4838 https://doi.org/10.3390/rs5104819.

Myneni, R.B., Keeling, C.D., Tucker, C.J., Asrar, G., Nemani, R.R., 1997. Increased plant growth in the northern high latitudes from 1981 to 1991. Nature 386 (6626), 698–702 https://doi.org/10.1038/386698a0.

Nemani, R.R., et al., 2003. Climate-driven increases in global terrestrial net primary production from 1982 to 1999. Science 300 (5625), 1560–1563. https://doi.org/10.1126/science.1082750.

O'Neill, B.C., et al., 2016. The scenario model intercomparison project (ScenarioMIP) for CMIP6. Geosci. Model Dev. 9 (9), 3461–3482 https://doi.org/10.5194/gmd-9-3461-2016.

Obermeier, W.A., et al., 2017. Reduced CO2 fertilization effect in temperate C3 grasslands under more extreme weather conditions. Nat. Clim. Chang. 7 (2) 137-+. https://doi.org/10.1038/Nclimate3191.

Pan, Y., et al., 2011. A large and persistent carbon sink in the world's forests. Science 333 (6045), 988–993 https://doi.org/10.1126/science.1201609.

Pascoe, C., Lawrence, B.N., Guilyardi, E., Juckes, M., Taylor, K.E., 2019. Designing and documenting experiments in CMIP6. Geosci. Model Dev. Discuss. 2019, 1–27 https://doi.org/10.5194/gmd-2019-98.

Peano, D., et al., 2019. Global variability of simulated and observed vegetation growing season. J. Geophys. Res. 124 (11), 3569–3587 https://doi.org/10.1029/2018jg004881.

Peñuelas, J., et al., 2013. Human-induced nitrogen–phosphorus imbalances alter natural and managed ecosystems across the globe. Nat. Commun. 4 (1) https://doi.org/10.1038/ncomms3934.

Piao, S.L., Fang, J.Y., He, J.S., 2006. Variations in vegetation net primary production in the Qinghai-Xizang Plateau, China, from 1982 to 1999. Clim. Change 74 (1–3), 253–267. https://doi.org/10.1007/s10584-005-6339-8.

Piao, S., Friedlingstein, P., Ciais, P., Zhou, L., Chen, A., 2006a. Effect of climate and CO2 changes on the greening of the Northern Hemisphere over the past two decades. Geophys. Res. Lett. 33 (23), L23402 https://doi.org/10.1029/2006 gl028205.

Piao, S., et al., 2018. Lower land-use emissions responsible for increased net land carbon sink during the slow warming period. Nat. Geosci. 11 (10) 739-+. https://doi.org/10.1038/s41561-018-0204-7.

Piao, S., et al., 2019. Characteristics, drivers and feedbacks of global greening. Nat. Rev. Earth Environ. 1 (1), 14–27 https://doi.org/10.1038/s43017-019-0001-x.

Pincus, R., Forster, P.M., Stevens, B., 2016. The radiative forcing model intercomparison project (RFMIP): experimental protocol for CMIP6. Geosci. Model Dev. 9 (9), 3447–3460 https://doi.org/10.5194/gmd-9-3447-2016.
Raftery, A.E., Gneiting, T., Balabdaoui, F., Polakowski, M., 2005. Using Bayesian model averaging to calibrate forecast ensembles. Monthly Weather Rev. 133 (5), 1155–1174 https://doi.org/Doi 10.1175/Mwr2906.1.
Reay, D.S., Dentener, F., Smith, P., Grace, J., Feely, R.A., 2008. Global nitrogen deposition and carbon sinks. Nat. Geosci. 1 (7), 430–437 https://doi.org/10.1038/ngeo230.
Reich, P.B., Hobbie, S.E., Lee, T.D., 2014. Plant growth enhancement by elevated CO2 eliminated by joint water and nitrogen limitation. Nat. Geosci. 7 (12), 920–924. https://doi.org/10.1038/ngeo2284. http://www.nature.com/ngeo/journal/v7/n12/abs/ngeo2284.html#supplementary-information.
Riahi, K., et al., 2017. The Shared socioeconomic pathways and their energy, land use, and greenhouse gas emissions implications: an overview. Glob. Environ. Chang. 42, 153–168 https://doi.org/10.1016/j.gloenvcha.2016.05.009.
Ribes, A., Planton, S., Terray, L., 2013. Application of regularised optimal fingerprinting to attribution. Part I: method, properties and idealised analysis. Clim. Dyn. 41 (11–12), 2817–2836 https://doi.org/10.1007/s00382-013-1735-7.
Sellers, P.J., 1985. Canopy reflectance, photosynthesis and transpiration. Int. J. Remote Sens. 6 (8), 1335–1372 https://doi.org/10.1080/01431168508948283.
Sellers, P.J., Berry, J.A., Collatz, G.J., Field, C.B., Hall, F.G., 1992. Canopy Reflectance, Photosynthesis, and Transpiration .3. A Reanalysis Using Improved Leaf Models and a New Canopy Integration Scheme. Remote Sens. Environ. 42 (3), 187–216 https://doi.org/Doi 10.1016/0034-4257(92)90102-P.
Sitch, S., et al., 2015a. Recent trends and drivers of regional sources and sinks of carbon dioxide. Biogeosciences 12 (3), 653–679 https://doi.org/10.5194/bg-12-653-2015.
Sitch, S., et al., 2015b. Recent trends and drivers of regional sources and sinks of carbon dioxide. Biogeosciences 12 (3), 653–679 https://doi.org/10.5194/bg-12-653-2015.
Stevens, N., Lehmann, C.E.R., Murphy, B.P., Durigan, G., 2017. Savanna woody encroachment is widespread across three continents. Glob. Chang. Biol. 23 (1), 235–244 https://doi.org/10.1111/gcb.13409.
Stouffer, R.J., et al., 2017. CMIP5 scientific gaps and recommendations for CMIP6. Bull. Am. Meteorol. Soc. 98 (1), 95–105 https://doi.org/10.1175/bams-d-15-00013.1.
Taylor, K.E., Stouffer, R.J., Meehl, G.A., 2012. An overview of cmip5 and the experiment design. Bull. Am. Meteorol. Soc. 93 (4), 485–498 https://doi.org/10.1175/bams-d-11-00094.1.
Sun, Y., et al., 2014. Rapid increase in the risk of extreme summer heat in Eastern China. Nat. Clim. Chang. 4 (12), 1082–1085. https://doi.org/10.1038/nclimate2410.
Taylor, K.R., 2001. Summarizing multiple aspects of model performance in a single diagram. J. Geophys. Res. 106 (D7), 7183–7192. https://doi.org/10.1029/2000JD900719.
Tebaldi, C., Knutti, R., 2007. The use of the multi-model ensemble in probabilistic climate projections. Philosophical Transactions of the Royal Society A: mathematical. Physical and Engineering Sciences 365 (1857), 2053–2075 https://doi.org/10.1098/rsta.2007.2076.
Van Auken, O.W., 2009. Causes and consequences of woody plant encroachment into western North American grasslands. J. Environ. Manage. 90 (10), 2931–2942 https://doi.org/https://doi.org/10.1016/j.jenvman.2009.04.023.
van der Ent, R.J., Savenije, H.H.G., Schaefli, B., Steele-Dunne, S.C., 2010. Origin and fate of atmospheric moisture over continents. Water. Resour. Res. 46 (9) https://doi.org/10.1029/2010wr009127.
Vautard, R., Cattiaux, J., Yiou, P., Thépaut, J.-N., Ciais, P., 2010. Northern Hemisphere atmospheric stilling partly attributed to an increase in surface roughness. Nat. Geosci. 3 (11), 756–761 https://doi.org/10.1038/ngeo979.
Vrugt, J., Diks, C., Clark, M., 2008. Ensemble Bayesian model averaging using Markov Chain Monte Carlo sampling. Environ. Fluid Mech. 8 (5–6), 579–595 https://doi.org/10.1007/s10652-008-9106-3.
Wang, R., et al., 2017. Global forest carbon uptake due to nitrogen and phosphorus deposition from 1850 to 2100. Glob. Chang. Biol. 23 (11), 4854–4872 https://doi.org/10.1111/gcb.13766.
Wang, X., et al., 2014. A two-fold increase of carbon cycle sensitivity to tropical temperature variations. Nature 506 (7487), 212–215 https://doi.org/10.1038/nature12915.
Xiao, Z., et al., 2014. Use of general regression neural networks for generating the GLASS leaf area index product from time-series MODIS surface reflectance. IEEE Trans. Geosci. Remote Sens. 52 (1), 209–223 https://doi.org/10.1109/tgrs.2013.2237780.
Xu, C., et al., 2019. Increasing impacts of extreme droughts on vegetation productivity under climate change. Nat. Clim. Chang. 9 (12), 948–953 https://doi.org/10.1038/s41558-019-0630-6.
Zanchettin, D., et al., 2016. The model intercomparison project on the climatic response to volcanic forcing (VolMIP): experimental design and forcing input data for CMIP6. Geosci. Model Dev. 9 (8), 2701–2719 https://doi.org/10.5194/gmd-9-2701-2016.
Zeng, Z., et al., 2017. Climate mitigation from vegetation biophysical feedbacks during the past three decades. Nature Clim. Chang. 7 (6), 432–436 https://doi.org/10.1038/nclimate3299.
Zeng, Z., et al., 2016. Responses of land evapotranspiration to Earth's greening in CMIP5 Earth System Models. Environ. Res. Lett. 11 (10), 104006 https://doi.org/Artn 10400610.1088/1748-9326/11/10/104006.
Zeng, Z.Z., et al., 2018. Impact of earth greening on the terrestrial water cycle. J. Clim. 31 (7), 2633–2650 https://doi.org/10.1175/Jcli-D-17-0236.1.
Zhou, L.M., et al., 2001. Variations in northern vegetation activity inferred from satellite data of vegetation index during 1981 to 1999. J. Geophys. Res.-Atmos. 106 (D17), 20069–20083.
Zhou, L., Kaufmann, R.K., Tian, Y., Myneni, R.B., Tucker, C.J., 2003. Relation between interannual variations in satellite measures of northern forest greenness and climate between 1982 and 1999. J. Geophys. Res.-Atmos 108 (D1). https://doi.org/10.1029/2002JD002510.
Zhu, Z., et al., 2013. Global data sets of vegetation leaf area index (LAI)3 g and fraction of photosynthetically active radiation (FPAR)3 g derived from global inventory modeling and mapping studies (GIMMS) normalized difference vegetation index (NDVI3g) for the period 1981 to 2011. Remote Sens (Basel) 5 (2), 927–948 https://doi.org/10.3390/rs5020927.
Zhu, Z., et al., 2017. Attribution of seasonal leaf area index trends in the northern latitudes with “optimally” integrated ecosystem models. Glob. Chang. Biol. 23 (11), 4798–4813 https://doi.org/10.1111/gcb.13723.
Zhu, Z., et al., 2016. Greening of the Earth and its drivers. Nat. Clim. Chang. 6 (8), 791–795 https://doi.org/10.1038/Nclimate3004.
Zhu, Z., et al., 2018. The accelerating land carbon sink of the 2000s may not be driven predominantly by the warming Hiatus. Geophys. Res. Lett. 45 (3), 1402–1409 https://doi.org/10.1002/2017GL075808.